JGR Planets

RESEARCH ARTICLE

10.1029/2020JE006724

Special Section:
Exoplanets: The Nexus of Astronomy and Geoscience

Structure and Thermal Evolution of Exoplanetary Cores

Irene Bonati[1], Marine Lasbleis[1,2], and Lena Noack[3]

[1]Earth-Life Science Institute, Tokyo Institute of Technology, Tokyo, Japan, [2]Laboratoire de Planetologie of Geodynamique, CNRS, Université de Nantes, Université d'Angers, Angers, France, [3]Department of Earth Sciences, Freie Universität Berlin, Berlin, Germany

Key Points:

- We investigate the evolution of the cores of rocky planets with masses 0.8–2 M_{Earth} and variable bulk and mantle iron contents
- The content and distribution of iron in a planetary body significantly influence core evolution and magnetic field lifetimes
- The cores of iron-rich planets tend to become fully solid, shutting off any pre-existing magnetic field and shortening the dynamo lifetime

Supporting Information:

Supporting Information may be found in the online version of this article.

Correspondence to:

I. Bonati,
irene.bonati@elsi.jp

Citation:

Bonati, I., Lasbleis, M., & Noack, L. (2021). Structure and thermal evolution of exoplanetary cores. *Journal of Geophysical Research: Planets*, *126*, e2020JE006724. https://doi.org/10.1029/2020JE006724

Received 5 OCT 2020
Accepted 9 APR 2021

Abstract Most of the large rocky bodies in the solar system display evidence of past and/or current magnetic activity, driven by thermochemical convection in an electrically conducting fluid layer. The discovery of a large number of extrasolar planets motivates the search for magnetic fields beyond the solar system. While current observations are limited to providing planetary radii and minimum masses, studying the evolution of exoplanets' magnetic fields and their interaction with the atmosphere can open new avenues for constraining interior properties from future atmospheric observations. Here, we investigate the evolution of massive rocky planets ($0.8 - 2\ M_{\mathrm{Earth}}$) with different bulk and mantle iron contents. Starting from their temperature profiles after accretion, we determine the structure of the core and model its subsequent thermal and magnetic evolution over 5 Gyr. We find that the planetary iron inventory and distribution strongly affect core structure, evolution, and the lifetime of a magnetic field. Planets with large bulk and mantle iron contents tend to feature large solid inner cores, which can grow up to the liquid outer core radius, shutting down any pre-existing magnetic activity. Consequently, the longest dynamo lifetimes ($\sim$ 4.25 Gyr) are obtained for massive planets with intermediate iron inventories. The smaller inner core radii and the chemical buoyancy fluxes introduced by the presence of light impurities can extend the magnetic field lifetimes to more than 5 Gyr. While the calculated magnetic fields are too weak to be detected by ground facilities, indirect observations may provide valuable insights into exoplanetary dynamos.

Plain Language Summary Earth's magnetic field is powered by vigorous convection in its liquid metallic outer core. The presence of a magnetic field is thought to accommodate habitable surface conditions by shielding the planetary upper atmosphere from harmful solar radiation. Most rocky planets in our solar system display past or present signatures of magnetic activity, and similar trends may exist in exoplanetary systems. The current knowledge of exoplanets relies on their radii and masses, while internal properties remain largely unconstrained. Studying the evolution of exoplanetary magnetic fields and their interaction with the surrounding environment will help to constrain interior properties from future atmospheric observations. Here, we investigate the structure and the thermal and magnetic evolution of the cores of rocky planets with different masses (0.8–2 Earth masses) and variable iron contents. We find that the iron content and its internal distribution between a planet's core and mantle strongly affect the evolution of the core and the lifetime of a magnetic field. The longest-lived magnetic fields are obtained for massive planets having intermediate iron contents. Iron-rich planets tend to grow fully solid cores, hindering any further magnetic activity. The presence of a small fraction of light core impurities can help prolong magnetic field lifetimes.

1. Introduction

Most of the large rocky bodies in the solar system present evidence of past and/or present magnetic activity (Breuer et al., 2010; Schubert & Soderlund, 2011; Stevenson et al., 1983), with the potential exception of Venus, for which no current magnetic field has been detected and no record of past activity is available (Dumoulin et al., 2017; Konopliv & Yoder, 1996; Nimmo, 2002; Zhang et al., 2016). Magnetic fields are generated through the dynamo mechanism in a large volume of an electrically conducting liquid in the planet's interior. Earth's magnetic field has been operating for about 3.45 Gyr (Tarduno et al., 2010) and is thought to be mainly sustained by the crystallization of its central solid inner core, powering thermo-chemical convection in the liquid outer core by the release of light-element enriched material and latent heat (Braginsky, 1963). The geodynamo is thus the result of the cooling of Earth's interior (Buffett, 2003; Labrosse, 2003), enhanced

by the presence of plate tectonics. In principle, the presence of a magnetic field is considered as evidence for a planet's internal dynamics, as well as for the existence of an electrically conducting layer at depth. While being a topic of active debate (Brain et al., 2013; T. E. Moore & Horwitz, 2007; Strangeway et al., 2010), planetary magnetism may also play an essential role in the development and long-term stability of habitable surface conditions, as it shields the upper atmosphere from mass loss induced by stellar winds and extreme space weather events (Dehant et al., 2007; Del Genio et al., 2020; Lammer et al., 2018).

The importance of magnetism for rocky planets' evolution and/or habitability strongly motivates the search and the study of magnetic fields beyond the solar system. To date, more than 4,000 exoplanets have been detected (Akeson et al., 2013; Schneider et al., 2011), with many bodies lying in the Earth and super-Earth regime, which is the focus of this study. Super-Earths are defined as rocky planets with masses larger than Earth but smaller than Neptune. Despite a large number of discovered exoplanets, knowledge regarding their internal structure is currently lacking (Baraffe et al., 2014; Spiegel et al., 2014), as current observations are limited to providing the planetary radius and/or its (minimum) bulk mass. While inferences on a planet's interior can be drawn to some degree, the internal structures and dynamic patterns matching these two constraints are manifold (Howe et al., 2014; Rogers & Seager, 2010). This degeneracy constitutes a significant barrier to obtaining unique solutions for planets' interior structures.

The ability of a planet to sustain habitable surface conditions is, however, strongly linked to its interior structure and dynamics (Noack et al., 2014). The detection and measurement of exoplanetary magnetic fields would help shed light on the internal structure and dynamics of extra-solar bodies, the frequency of planetary magnetic fields in the Universe, and the importance of magnetic activity for the emergence of planetary habitability. No direct detection of magnetic fields beyond our solar system exists to this date, and observations remain challenging due to the limited sensitivity of current instrumentation, which is too low to detect the weak magnetic fields exerted by small rocky planets (Driscoll & Olson, 2011). Upcoming missions aimed at investigating exoplanetary atmospheres (e.g., JWST, ARIEL, WFIRST) will enable additional characterization of exoplanetary bodies (Gardner et al., 2006; Spergel et al., 2015). Until then, theoretical modeling can provide a means for understanding and constraining the interactions between a planet's interior and its atmosphere. Magnetic fields are well suited for this purpose, as they span a planet in its entirety, being generated in the deepest portion of the interior and manifesting in the upper layers of the atmosphere.

Past modeling efforts investigating exoplanetary interiors have led to the development of simple scaling laws for deriving the internal structures (i.e., the core and planetary radius) and dynamic properties (likelihood of plate-tectonics-like behavior) of super-Earths (Seager et al., 2007; Valencia et al., 2006). These relations often assume a core-mantle boundary (CMB) heat flux proportional to the planetary mass and an Earth-like composition. Recent work by Boujibar et al. (2020) provided internal structures of super-Earths at the end of accretion using newly developed core and mantle melting temperatures (Stixrude, 2014) and predicted that massive bodies are likely to feature partially solid cores. Scaling laws providing estimates for the magnetic field intensity at the CMB based on the available energy for dynamo generation have been devised as well (Aubert et al., 2009; Olson & Christensen, 2006), and have been extensively used by both the geophysical and the planetary science communities (e.g., Driscoll & Olson, 2011; López-Morales et al., 2011; McIntyre et al., 2019).

Studies investigating the ability of massive rocky planets to sustain dynamo activity have reached contrasting results. Gaidos et al. (2010) predicted that planets more massive than 2 M_{Earth} do not feature dynamos due to the flattening of the temperature slope of the iron solidus with respect to the core adiabat. This scenario would predict iron snow to form, but the latent heat release is not high enough to drive dynamo action. Tachinami et al. (2010) also found dynamo activity to be unlikely for high mass planets due to the high lower mantle viscosities and the small temperature jumps at the CMB. Driscoll and Olson (2011) have considered optimal conditions (i.e., efficient cooling of the core across the CMB and vigorous convection in the core and mantle) for dynamo generation in $1 - 10\ M_{\mathrm{Earth}}$ planets and have shown that thermal convection can sustain strong magnetic fields on massive exoplanets. Similarly, van Summeren et al. (2013) predict that Earth-mass planets (and potentially massive exoplanets) with plate tectonics can have strong magnetic fields persisting over billions of years compared to bodies in a stagnant lid configuration.

Core fractions of planets modeled in the above studies are equivalent to those of solar system bodies (Earth, Mercury, and Mars). However, depending on their mass and composition, planets can cover a large variety of possible core structures and sizes, which can have strong implications for the likelihood and the longevity of the generated magnetic fields (Driscoll & Olson, 2011). This diversity results from different disk compositions (Bond et al., 2010; Moriarty et al., 2014), accretion processes, and the planetary differentiation history. In addition, the distribution of iron between the core and the mantle, which is strongly related to accretion and differentiation (Elkins-Tanton & Seager, 2008; Wohlers & Wood, 2017), has substantial implications for the planetary structure, as well as for the melting temperatures, viscosity, thermodynamic and transport properties such as electric conductivity, and the resulting dynamics of the mantle and core. This effect has been investigated in a recent study by Noack and Lasbleis (2020), who provided parameterizations for the internal structures of rocky planets having different masses and iron contents.

Here, we investigate the evolution of the core of rocky bodies with variable masses and iron contents (bulk and mantle), assuming an Earth-like composition. Starting from their internal structure after the solidification of molten silicates at the CMB (Noack & Lasbleis, 2020; Stixrude, 2014), we determine the initial core structure and model its subsequent thermal and magnetic evolution by computing inner core growth, buoyancy fluxes, and the strength and lifetime of the generated magnetic field. The manuscript is structured as follows: In Section 2 we briefly introduce the interior structure and the mantle evolution model (Section 2.1), as well as the thermal evolution model for the core (Section 2.2). We then present core structures (Section 3.1) and evolution histories (Section 3.2) obtained by varying the planetary mass and the bulk and mantle iron contents, as well as the fraction of light alloying components in the core. We show the calculated magnetic field strengths and lifetimes in Section 3.3. In Section 4 we discuss our results and parameter uncertainties. A summary can be found in Section 5 together with some concluding remarks.

2. Methods

2.1. Interior Structure and Mantle Evolution Model

We obtain internal structures from the code Code for Habitability, Interior and Crust (CHIC; Noack et al. [2017]), which contains modules for the 1-D internal profiles and mantle convection (described in Section 2.1.4). Structures are calculated for planets with variable masses and iron contents, leading to different core mass fractions. The explored planetary mass range lies between 0.8 and 2 M_{Earth} (with $M_{\mathrm{Earth}} = 5.972 \cdot 10^{24}$ kg being Earth's mass). We employ bulk weight fractions of iron X_{Fe} between 0.15 and 0.8 (15–80 wt.% Fe: as a reference, Earth has an iron content of about 32 wt.%), and mantle iron numbers $\#Fe_{\mathrm{M}}$ varying between 0 and 0.2 (as a reference, Earth has a mantle iron number $\#Fe_{\mathrm{M}}$ of 0.1). The mantle iron number is defined as the molar ratio between iron-bearing (FeO, $FeSiO_3$ and Fe_2, SiO_4) and magnesium-rich minerals (MgO, $MgSiO_3$ and Mg_2 SiO_4). The range explored in this study ($\#Fe_{\mathrm{M}} = 0 - 0.2$) corresponds to mantle iron mass fractions $X_{\mathrm{Fe,\,m}} = 0 - 0.1457$ (see also Noack and Lasbleis (2020)). The interior structure model solves the hydrostatic, Poisson, and mass conservation equations from the planetary center to its surface in order to obtain internal pressure, gravity, and mass profiles. The planetary surface pressure is set to 1 bar. Using the planetary mass and the iron contents X_{Fe} and $\#Fe_{\mathrm{M}}$ as inputs, the model determines the planetary structure (core and planetary radius) and the thermodynamic parameter profiles self-consistently.

The model assumes Earth-like rock-forming elements (Mg, Fe, Si, and O) and mineral assemblages (olivine, wadsleyite, ringwoodite, bridgmanite, magnesiowüstite, and post-perovskite). The mantle consists of $(\mathrm{Mg}_{1-\#Fe_{\mathrm{M}}}, \mathrm{Fe}_{\#Fe_{\mathrm{M}}})\mathrm{O}$ and SiO_2, where an Earth-like elemental ratio of Mg, Fe, Si, and O in the mantle corresponds to a mantle iron number $\#Fe_{\mathrm{M}} = 0.1$. Even though some exoplanets might be rich in other elements (e.g., aluminum, calcium, carbon) and display different chemistries (Dorn, Harrison, et al., 2019; Kuchner & Seager, 2005; Madhusudhan et al., 2012; Miozzi et al., 2018), it is likely for planetary building blocks located inside the snow line to have mineralogies similar to planets in the inner solar system, with slight variations in the Mg, Fe, and Si contents depending on the host star's metallicity (Bitsch & Battistini, 2020). A third-order Birch-Murnaghan (Stixrude & Lithgow-Bertelloni, 2011) and a Holzapfel (Bouchet et al., 2013) equations of state are used for the mantle and the core (pure iron), respectively. Interior structures of planets with masses beyond 2 M_{Earth} are not explored, as the employed equations of state are devised for Earth's pressure range, and extrapolating to higher pressures would lead to errors due to missing data

from experiments and ab initio simulations. We therefore set the upper planetary mass limit to 2 M_{Earth}, for which robust equations of state for both mantle and core are available (Hakim et al., 2018). For more details about the interior structure model, the reader is redirected to the paper by Noack, Rivoldini, and Van Hoolst (2017), and to Noack and Lasbleis (2020) for the parameterizations of interior properties of massive rocky planets.

2.1.1. Thermal Profiles of the Core

Recent studies have stressed the importance of both the initial structure and the thermal profile of a planet, as they set the stage for its subsequent evolution and tectonic behavior (Breuer et al., 2010; Dorn, Noack, & Rozel, 2018; O'Neill et al., 2016; Stamenković & Breuer, 2014; Stamenković et al., 2012; Stein et al., 2004). Estimating the energy budget of bodies during and in the aftermath of accretion is challenging, even for planets in the solar system. This is due to the many unconstrained thermodynamic and transport parameters. Here, we use initial temperature profiles corresponding to the "hot" scenarios in Noack and Lasbleis (2020). These are high-temperature end-members of the profiles in Stixrude (2014), determined for planets with an Earth-like composition and variable mass. These profiles describe planets at the late stage of planet formation, right after the full crystallization of the silicates at the CMB. The solidified material could be a portion of a (global) magma ocean, which is likely to be present in the aftermath of accretion (Abe, 1997; Canup, 2004; Nakajima & Stevenson, 2015). Typically, solidification of a magma ocean proceeds from the bottom of the mantle toward the surface (Andrault et al., 2011; Monteux et al., 2016), but middle-out crystallization processes, potentially leading to the preservation of a basal magma ocean for billions of years, have been proposed as well (Labrosse, Hernlund, & Coltice, 2007; Nomura et al., 2011; Stixrude et al., 2009).

2.1.2. Melting Curves and Inner Core Size

We use formulations for the melting curves of iron and rock components in super-Earths interiors similar to those proposed in Stixrude (2014), which are based on existing experimental results, ab initio data, and scaling laws. The melting temperature of the mantle for pressures $P > 17$ GPa is defined as

$$T_{\text{m, mantle}} = 5400\left(\frac{P}{140 \cdot 10^9}\right)^{0.48} \frac{1}{1 - \ln(1 - \#Fe_{\text{M}} - X_{\text{M}})}. \quad (1)$$

with pressure P in Pascal and temperature T in Kelvin. X_{M} is a scaling factor indicating the difference between the liquidus and solidus temperatures. As stated previously, the mantle iron number $\#Fe_{\text{M}}$ defines the ratio between iron and magnesium-bearing minerals present in the mantle, which are assumed to be similar to Earth. An increase of $\#Fe_{\text{M}}$ leads to a reduction of the mantle melting temperature $T_{\text{m, mantle}}$. Similarly, the mantle melting temperature decreases with varying mantle composition, reflected by the parameter X_{M}. The melting temperature reduction is parameterized with $X_{\text{M}} = 0.11$ and $\#Fe_{\text{M}} = 0.1$ to reflect the observed mantle melting temperature variations in the literature as estimated for bridgmanite (with a rather low influence on melting temperatures, Zerr and Boehler (1993)) and magnesiowüstite (with melting temperature variations between two and four thousand Kelvin for $\#Fe_{\text{M}} = 0$ and $\#Fe_{\text{M}} = 0.2$ following Fu et al. (2018) and Boukaré et al. (2015)), and to match Earth-like melting temperatures for $\#Fe_{\text{M}} = 0.1$ (Stixrude, 2014). We refer to this as the "warm" profile (mimicking a planetary evolution stage at which the CMB temperature is equal to the mantle solidus). Conversely, the case with $X_{\text{M}} = 0$ is referred to as the "hot" profile (mimicking an evolution stage at which the CMB temperature matches the mantle liquidus). We note that our parameterization for the influence of iron on melting temperatures directly impacts the initial core temperatures calculated in Noack and Lasbleis (2020). A stronger influence of iron on melting temperatures than parameterized here (as observed, for example, for magnesiowüstite) would lead to colder initial core temperatures for higher mantle iron numbers, making the magnetic activity less likely than observed in our results.

The melting temperature for pure iron in Stixrude (2014) is based on Morard, Bouchet, et al. (2011), and is defined as

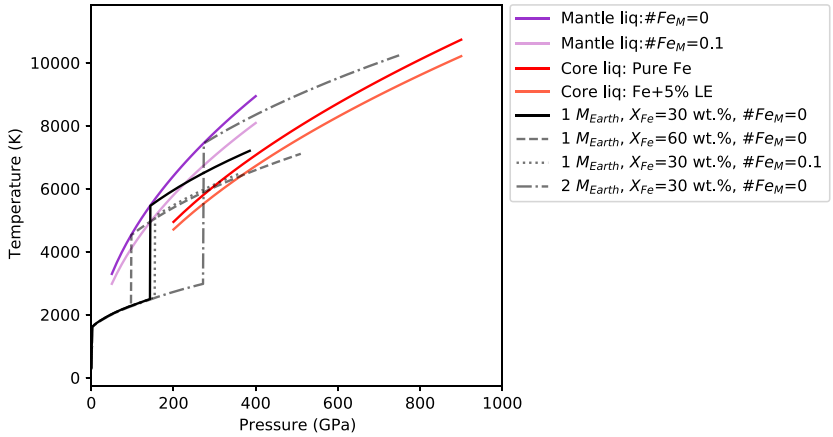

Figure 1. Initial temperature profiles for planets with masses of 1 and 2 M_{Earth}, bulk iron contents X_{Fe} of 30 wt.% and 60 wt.%, and mantle iron numbers $\#Fe_{\mathrm{M}}$ of 0 and 0.1. The purple and red solid lines display mantle liquidus curves for different mantle iron numbers ($\#Fe_{\mathrm{M}}$ of 0 and 0.1) and core liquidus curves for different core compositions (a pure iron core and a core containing iron and 5% of light elements), respectively. All profiles are consistent with the "hot" scenarios in Noack and Lasbleis (2020), following which the temperature at the CMB is anchored to the mantle liquidus.

$$T_{\mathrm{m,core}} = 6500\left(\frac{P}{340\cdot 10^{9}}\right)^{0.515}\frac{1}{1-\ln(1-x)}, \tag{2}$$

where P is the pressure (in Pa) and x is the mole fraction of light components in the core. The dependence on x in Equation 2 reflects the reduction of the core melting temperature due to the presence of light elements. Earth's outer core is thought to contain about 5–10% of light elements, which were imparted during accretion and core formation (Badro et al., 2015; Rubie et al., 2011; Wood et al., 2006). The presence of light elements in Earth's core compensates for the temperature jump at the inner core boundary (ICB), which does not correspond to a pure phase change (Badro et al., 2015; Hirose et al., 2013). Although the identities and contributions of these components remain unconstrained, seismology and mineral physics studies have proposed oxygen, silicon, sulfur, carbon, and hydrogen as potential candidates (Hirose et al., 2013). Light elements may be present in the cores of massive exoplanets as well, although the identification of likely candidates and their partitioning properties at high pressures require further investigation. For this study, we vary the core light element content between 0% and 10% and assume that light components preferentially partition into the liquid outer core during evolution.

The employed melting temperatures for the mantle and the core are shown together with the thermal profiles in Figure 1, for planets of 1 and 2 M_{Earth} with variable bulk iron contents X_{Fe} (30 wt.% and 60 wt.%) and mantle iron numbers $\#Fe_{\mathrm{M}}$ (0 and 0.1). The mantle and core melting temperatures are reduced with the addition of iron and light impurities, respectively. The thermal profiles are high-temperature end-member scenarios of the ones in Stixrude (2014) and correspond to the "hot" scenarios in Noack and Lasbleis (2020), where the uppermost core temperature is anchored to the mantle liquidus, which varies according to the mantle iron content. The temperature jump at the CMB is calculated for every planet depending on its internal structure and thermodynamic parameters (see Noack & Lasbleis [2020] for further details).

2.1.3. Polynomial Fitting of Interior Profiles

Noack and Lasbleis (2020) provided a suite of parameterizations for average thermodynamic parameters in planetary mantles and cores. In order to model the evolution of the metallic core, the pressure-dependent density profile is required. Following the work of Labrosse (2015) of fitting the Preliminary Reference Earth Model (PREM) for the Earth, we fit the initial interior profiles obtained using the model described in Section 2.1. We fit the core density by using a polynomial function with three parameters: the density at the planetary center ρ_0, the typical length scale for density variations L_ρ, and a second-order variation A_ρ as

$$\rho(r) = \rho_0 \left(1 - \frac{r^2}{L_\rho^2} - A_\rho \frac{r^4}{L_\rho^4}\right) \tag{3}$$

with

$$L_\rho = \sqrt{\frac{3K_0}{2\pi G \rho_0^2}}; \quad A_\rho = \frac{5K_0^{'} - 13}{10}, \tag{4}$$

where $K = K_0 + K_0'(P - P_0)$ is the bulk modulus, which is considered pressure-dependent and is anchored at the planetary center (radiolabeled by the subscript 0), and G is the gravitational constant ($G = 6.67430 \cdot 10^{-11}$ m^3 kg^{-1} s^{-2}). Values of L_ρ and A_ρ, obtained for planets of different mass and bulk iron content, are shown in Figure S1. P_0 and K_0' are the pressure and the pressure derivative of the bulk modulus at the planetary center, respectively.

Integrating the gravity using Gauss' theorem and assuming the system is in hydrostatic equilibrium, the gravity and pressure profiles $g(r)$ and $P(r)$ are

$$g(r) = \frac{4\pi}{3} G \rho_0 r \left(1 - \frac{3}{5}\frac{r^2}{L_\rho^2} - \frac{3A_\rho}{7}\frac{r^4}{L_\rho^4}\right), \tag{5}$$

$$P(r) = P_0 - K_0 \left(\frac{r^2}{L_\rho^2} - \frac{4}{5}\frac{r^4}{L_\rho^4}\right). \tag{6}$$

The expression for P is given up to order 4. K_0 is obtained from Equation 4

$$K_0 = \frac{2}{3}\pi L_\rho^2 \rho_0^2 G. \tag{7}$$

We assume that the core density does not evolve with time, although light elements are expelled into the liquid phase as a solid inner core grows, which should cause a variation on the order of a few percents. As a result, we neglect both the thermal and chemical dependence of the density compared to the one related to pressure variations. The temperature profile $T(r)$ is assumed to be isentropic, that is, with γ being the Grüneisen parameter,

$$\left(\frac{\partial \ln(T)}{\partial \ln(\rho)}\right)_S = \gamma. \tag{8}$$

Anchoring this temperature profile to the radius r_0 with density $\rho(r_0)$, and assuming a constant γ, the temperature profile is given by

$$T(r) = T(r_0)\left(\frac{\rho(r)}{\rho(r_0)}\right)^\gamma. \tag{9}$$

The value of γ is obtained by averaging the Grüneisen parameter over the core volume, which varies only by a few percentages in our models (maximum of 6% for the largest planets featuring the largest cores). We expect the variations with temperature to be negligible. The radius r_0 is chosen as either the planetary center (i.e., $r_0 = 0$) when there is (still) no inner core, or the inner core radius r_{IC} once the inner core starts forming (see Section 2.2 for more details).

2.1.4. Mantle Thermal Evolution Model

Starting from the temperature profiles shown in Figure 1, based on Noack and Lasbleis (2020), we simulate the long-term thermal evolution of the mantle over 5 Gyr. Based on the heat loss from the mantle to the

surface by convection and conductive heat flow, we can estimate how strong the core cools and how the heat flux at the CMB varies over time. Estimating the evolution of the heat flow at a planet's CMB is challenging. For the Earth, estimates of the present CMB heat flow range between ~ 5–17 TW (Lay et al., 2008), and its lateral variation and evolution remain unclear. As a result, past work has assumed either a linearly or exponentially decaying CMB heat flow (Labrosse, 2003, 2015). However, the frequency of time-dependent geomagnetic reversals excludes both, meaning that an oscillatory CMB heat flux is preferred (Olson et al., 2013).

We employ the mantle convection code CHIC (Noack et al., 2017) to obtain the CMB heat flow for planets of different mass and iron contents (bulk and mantle). The model solves the conservation equations for mass, momentum, and energy in a 2-D quarter sphere using the spherical annulus geometry (Hernlund & Tackley, 2008), which reproduces thermal evolution scenarios similar to a 3-D sphere while using much less computational power. We model compressional convection under the truncated anelastic liquid approximation (TALA), where thermodynamic reference profiles for parameters such as density, thermal expansion coefficient, and heat capacity are calculated as described in Noack and Lasbleis (2020).

The mantle is heated by radioactive decay and core cooling. The heat flux of the core-mantle boundary is determined only from the mantle side, assuming that the thick thermal boundary forming at the bottom of the mantle dictates how much heat flows into the mantle from the core. The core is not considered for mantle evolution, meaning that no energy contribution from core freezing (latent heat, gravitational energy) is taken into account. The obtained CMB heat flow is used *a posteriori* to compute the energy inputs resulting from secular cooling, latent heat, and gravitational heat release (Equation 10) at different stages of evolution (Nakagawa & Tackley, 2010, 2013), but is not taken into account for the mantle evolution simulations. The thermal conductivity of the mantle changes with pressure according to Tosi et al. (2013).

The modeled planets are in a stagnant lid tectonic configuration, featuring a unique rigid plate that does not break up and sink into the mantle in a subduction-like manner. We consider melt formation in the upper mantle, which directly impacts the thermal evolution of the mantle due to latent heat consumption upon melting. We assume that melt that is buoyant enough (i.e., for pressures below 12 GPa, Ohtani et al. [1995]) is immediately transported to the surface and separated from the convecting mantle by a stagnant lithosphere. Note that for small degrees of melting (i.e., for melt fractions of 1%–3%; Fraeman & Korenaga [2010]), the melt may remain in the mantle. We do not take this into account in the current study, but the effect on the long-term evolution of the mantle should be minor since melting with larger melt fractions would be extracted toward the surface. As the melt rises upwards, its composition, the density contrast with the surrounding material, and the melt viscosity dictate what fraction of the melt erupts at the surface and what portion recrystallizes intrusively. Here, we do not follow the extraction of melt or the influence of recrystallization within the crust (potentially leading to a plutonic-squishy lid, Lourenço et al. [2020]), nor the sinking of overlying crustal material (heat-pipe model, W. B. Moore & Webb [2013]), as we are mainly interested in the deep mantle thermal evolution. Furthermore, if plate tectonics were considered, subduction of the cooler lithosphere into the mantle would lead to additional cooling of the mantle, triggering higher heat fluxes at the CMB than modeled here. However, it is yet unclear how likely plate tectonics is on rocky planets, as Earth is the only rocky body we know of so far that experiences plate tectonics (though speculations exist for its sister planet, Venus). Furthermore, Stamenković et al. (2012) showed that at least for super-Earths, the heat flux at the CMB is not affected by the surface mobilization regime since a strong cooling of the upper mantle leads to a decoupling of the upper and lower part of the mantle, leading to similar long-term heat flux patterns at the CMB. For this reason, we limit our study to stagnant-lid planets.

Here, we consider an Earth-like radiogenic abundance in the mantle (McDonough & Sun, 1995). However, radiogenic heat production affects how much heat is extracted at the core-mantle boundary, thus influencing the occurrence of core convection and dynamo action (Nimmo et al., 2020). A higher degree of radioactivity may decrease the heat flow from the core to the mantle and lead to shorter magnetic field lifetimes than calculated here. Radioactive isotopes are also a significant heat source for the mantle. The presence of radioactive heat sources increases the mantle temperature, triggering more upper mantle melting and volcanic outgassing (Dorn et al., 2018). On the other hand, for a hotter mantle, convection becomes more vigorous, leading to more efficient heat transport toward the surface and efficient mantle cooling. Similarly, increased mantle melting can effectively reduce mantle energy due to latent heat consumption

upon melting. Therefore, radiogenic heat sources tend to lead to slower core cooling and a decreased CMB heat flow, but counter-effects by vigorous convection and melting may reduce its impact on the long-term evolution of the core.

One of the most important factors impacting the thermal evolution of the mantle is the viscosity of the silicate rocks, which depends on temperature, pressure, and composition. A hotter mantle tends to have a lower viscosity promoting vigorous convection and heat transport toward the surface. In turn, this leads to a smaller temperature jump at the core-mantle boundary, decreasing the amount of heat extracted from the core. On the other hand, a cooler lower mantle displays a higher viscosity due to its strong temperature dependence. Viscosity variations thus have a strong impact on convective strength and volcanic activity (Dorn et al., 2018,). Water content also plays a crucial role. A hydrated upper mantle, for example, is expected to display a viscosity reduction of about two orders of magnitude when compared to a dry mantle (Karato & Wu, 1993). Similarly, the mineral composition can strongly influence viscosity as well. For example, a MgO-rich mantle is much weaker than a $MgSiO_3$-dominated mantle (Yamazaki & Karato, 2001). Finally, an increased iron content leads to a viscosity reduction, even though the variation is of less than one order of magnitude with respect to $\#Fe_M = 0.1$ for the small range of mantle iron numbers investigated here ($\#Fe_M = 0.1 \pm 0.1$; Zhao et al. (2009)). In the present study, we consider mantle viscosity to vary with temperature and pressure, but we do not take chemical effects into account. We assume silicate rocks to be dry but otherwise Earth-like (Noack et al., 2017), and use the viscosity laws from Karato and Wu (1993) for the upper mantle and from Tackley et al. (2013) for the lower mantle. The extent to which temperature and pressure effects influence viscosity as compared to chemistry is still unconstrained. Tackley et al. (2013) have shown that for planets more massive than Earth, a self-lubricating viscosity tends to evolve in the lower mantle, with lower viscosities leading to more efficient heat removal from the lower mantle toward the upper mantle, resulting once again in a higher viscosity. This result indicates that chemical variations of the viscosity may be balanced by thermal effects to achieve steady convection in the lower mantle. Future studies will need to infer the interplay between composition, pressure, and temperature on viscosity profiles in the deep mantle for planets of different masses. Since we are interested in the long-term thermal evolution of the mantle rather than local convective features, we use a coarse radial resolution of 50 km, with a similar average lateral resolution (but varying with radius due to the spherical shape of the mantle) to save computational costs. As shown in Dorn et al., (2018), the mantle resolution (which goes down to a radial resolution of 10 km in that study) does not have a strong effect on the thermal evolution of the mantle.

Since the focus of our study lies on the comparative aspect of core and magnetic field evolution depending on planet mass and iron content, we applied a simplified reference mantle evolution model (e.g., using Earth-like radiogenic heat sources; immediate extraction of melt to the surface; viscous rheology not taking plasticity into account). We refer to mantle evolution studies that investigated the impact of such factors on the long-term evolution of the mantle (; Dorn et al., 2018; Noack et al. 2017; O'Neill et al., 2016, Tackley et al., 2013), which goes beyond the scope of our study. We assume that the general trends that we observe for core cooling and magnetic field lifetimes depending on planet mass and iron content would not change dramatically when applying a different mantle evolution model but would instead lead to a shift in the magnetic field longevity.

2.2. Core Evolution Model

2.2.1. Energy Balance

Starting from the initial profiles described in Section 2.1, we model the subsequent thermal and magnetic evolution of the core for planets of different mass and iron contents (bulk and mantle). To do this, we design a 1-D parameterized model tracking inner core growth and calculating the core energy budget, the buoyancy fluxes, and the magnetic dipole moment. This is performed using an energy balance approach, which has been extensively used in past studies investigating the geodynamo (Braginsky & Roberts, 1995; Driscoll & Bercovici, 2014; Gubbins, 1977; Labrosse, 2003, 2015; Lister & Buffett, 1995; Nimmo, 2007; Nimmo & Schubert, 2015). The main concept behind energy balance models is that the heat flow at the CMB, Q_{CMB}, is equal to the sum of the secular cooling of the outer core Q_C, the latent heat from the freezing of the inner core Q_L, the gravitational heat due to the light element release at the ICB Q_G, and heat generated from radioactive decay Q_R (see Figure 2) as

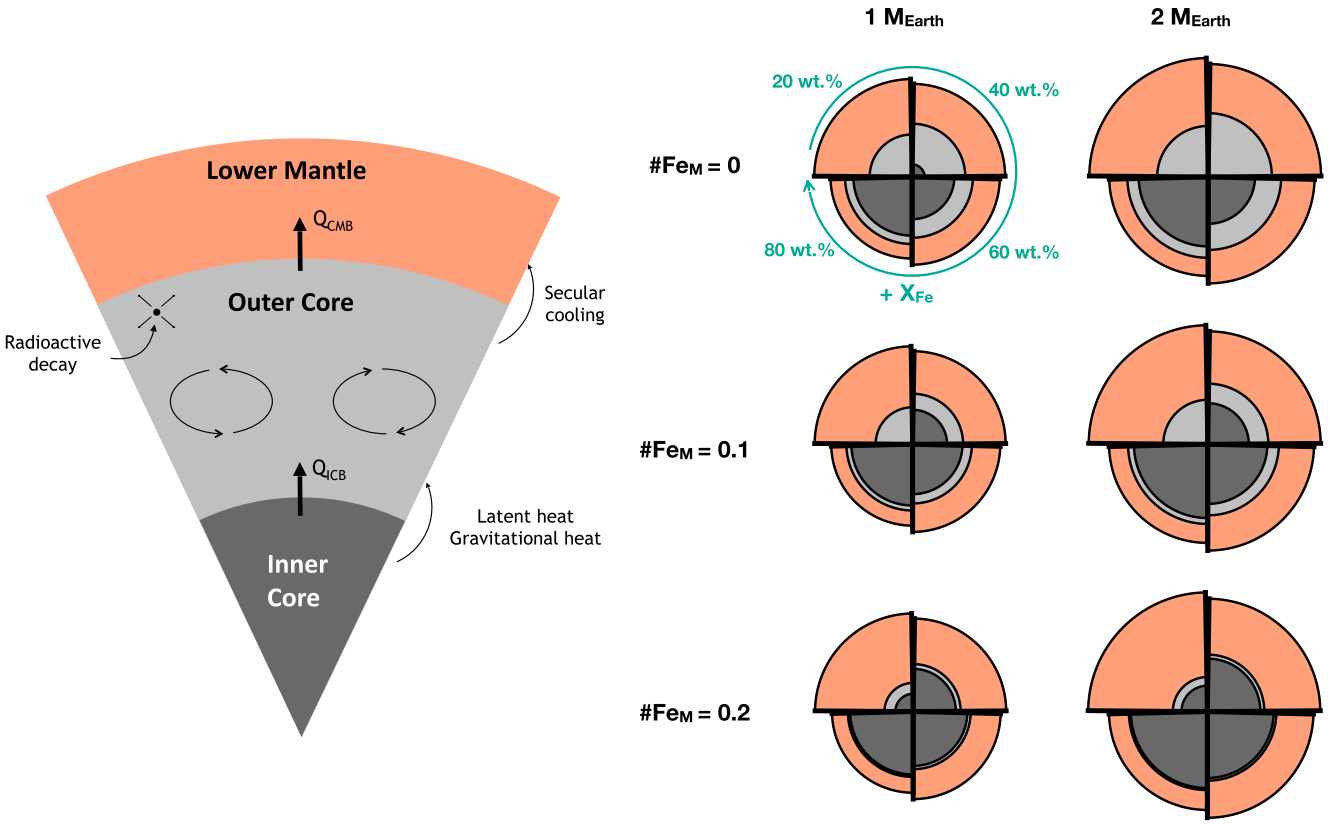

Figure 2. (left) Schematic representation of a planetary interior showing the solid inner core, the liquid outer core, and a portion of the viscous lower mantle. As the inner core solidifies, it releases heat into the outer core in the form of latent and gravitational heat. In turn, the outer core releases heat into the mantle due to secular cooling. All these energy contributions drive convection in the outer core and power dynamo activity. (right) Internal structures calculated for planets with different masses (1 and 2 M_{Earth}) and iron contents at the end of accretion, right after the crystallization of molten silicates at the CMB. From top to bottom, the mantle iron number $\#Fe_M$ is 0, 0.1, and 0.2. The bulk iron inventory X_{Fe} increases in a clockwise direction (20, 40, 60, and 80 wt.% Fe in the upper left, upper right, lower right, and lower left quarters, respectively). CMB, core-mantle boundary.

$$Q_{CMB} = Q_C + Q_L + Q_G + Q_R \tag{10}$$

We assume that the heat produced by radioactive decay Q_R is negligible, as is often done for Earth. The abundance of radioactive elements in planetary cores is not well constrained. Potassium is moderately soluble in iron during core formation (Lee & Jeanloz, 2003), and small amounts of uranium and thorium may enter the core as well (Blanchard et al., 2017; Chidester et al., 2017, e.g.). Core radioactivity acts as an additional heat source and may aid the persistence of a dynamo, likely extending the magnetic field lifetimes obtained here. While a fraction of radioactive elements may be present in planetary cores, their identity and contribution to the energy budget of a planet's core and dynamo action require further investigation. The model is run for 5 Gyr of a planet's evolution, which is a reasonable time interval given current distributions of stellar ages (Frank et al., 2014; Safonova et al., 2016).

2.2.2. Before Crystallization of an Inner Core

In the absence of an (initial) inner core, and neglecting the heat produced by radioactive decay, the energy balance before inner core crystallization can be simply expressed as $Q_{CMB} = Q_C$, where the secular cooling Q_C is defined as

$$Q_C = -\int_{V_C} \rho C_P \frac{\partial T_a}{\partial t} dV. \tag{11}$$

Here, V_C is the volume of the core, C_P is the specific heat capacity of the core, T_a is the adiabatic temperature, and t is time. The adiabatic temperature profile is defined as in Equation 9, and is anchored at the planetary center $r_0 = 0$ with density ρ_0, as

$$T_a(r,t) = T_0(t)\left(1 - \frac{r^2}{L_\rho^2} - A_\rho \frac{r^4}{L_\rho^4}\right)^\gamma, \tag{12}$$

where T_0 is the temperature at the planetary center. Q_C then becomes

$$Q_C = -4\pi\rho_0 C_p \frac{dT_0}{dt} \int_0^{r_{OC}} \left(1 - \frac{r^2}{L_\rho^2} - A_\rho \frac{r^4}{L_\rho^4}\right)^{\gamma+1} r^2 dr. \tag{13}$$

The integral can either be approximated numerically, or by applying the development described in Eq. A2 in Labrosse (2015). We introduce the notation

$$f_C(r,\delta) = 3\int_0^r (1 - r^2 - A_\rho r^4)^{1+\delta} r^2 dr, \tag{14}$$

so that the secular cooling term can be written as

$$Q_C = -\frac{4}{3}\pi\rho_0 C_P L_\rho^3 f_C\left(\frac{r_{OC}}{L_\rho}, \gamma\right)\frac{dT_0}{dt}. \tag{15}$$

Q_C can be rewritten as $Q_C = P_C \frac{dT_0}{dt}$, where P_C is a constant which depends on the global parameters of the core and does not vary with time. The temperature at the center can finally be written as

$$T_0(t) = T_0(t=0) + \frac{1}{P_C}\int_0^t Q_{CMB}(\tau) d\tau. \tag{16}$$

Here, Q_{CMB} is the CMB heat flux obtained using the model of Noack et al., (2017). Inner core crystallization starts when the temperature at the planetary center reaches the liquidus temperature of the outer core alloy, neglecting the possible existence of supercooling effects (Huguet et al., 2018).

2.2.3. After Crystallization of an Inner Core

In addition to the secular cooling term, the energy balance after the onset of inner core solidification needs to account for latent and gravitational heat release (Equation 10). These terms can be written as

$$Q_C = -\int_{V_{OC}} \rho C_P \frac{\partial T_a}{\partial t} dV, \tag{17}$$

$$Q_L = 4\pi r_{IC}^2 \rho(r_{IC}) T_{m,core}(r_{IC}) \Delta S \frac{dr_{IC}}{dt}, \tag{18}$$

$$Q_G = -\int_{V_{OC}} \rho\mu' \frac{\partial X}{\partial t} dV. \tag{19}$$

Here, V_{OC} is the volume of the outer core, $T_{m,core}(r_{IC})$ and $\rho(r_{IC})$ are the melting temperature and the density at the ICB, ΔS is the entropy of freezing (set to 127 $Jkg^{-1}K^{-1}$; Hirose et al. [2013]), μ' is the difference between the adiabatic and the chemical potentials at the ICB (see Labrosse [2015] for a more detailed derivation), and $\frac{\partial X}{\partial t}$ is the temporal change of light element mass fraction in the outer core. We calculate the melting temperature of the outer core alloy at the inner core radius $r_{IC}(t)$ according to Equation 2 to obtain the temperature change at the ICB. The temperature at the CMB is assumed to lie on the adiabatic profile, consistent with vigorous convection. Similar to what was previously shown for a planet with no inner core

(Section 2.2.2), we can write each of the terms in Equation 17, (18), and (19) as $Q_X = P_X \frac{dr_{IC}}{dt}$, where X indicates a given heat contribution (secular cooling, latent heat or gravitational heat). The P_X terms for these different contributions are presented in the Supplementary Information of this paper. We write them similarly as in Labrosse (2015), and redirect the reader to the Appendix of that study for further details.

2.3. Change of Outer Core Composition

If the core contains light elements, its composition will evolve as the inner core solidifies due to the gradual release of these impurities. Seismic velocity anomalies in Earth's core hint at the presence of 5–10% light components (Badro et al., 2015; Hirose et al., 2013), candidates of which are oxygen, silicon, sulfur, carbon, and hydrogen (Poirier, 1994). While their abundance and identity are unconstrained, it is likely for such impurities to be present in the cores of massive exoplanets.

Here we use light element bulk contents ranging between 0–10%. Depending on whether there is an inner core or not, the inventory of light elements in the outer core will differ and is larger for bodies featuring larger solid inner cores. With $M_{OC}(t)$ being the mass of the outer core, M_C the mass of the core, and X_0 the bulk fraction of light elements in the outer core in the absence of an inner core, we can obtain the fraction of light elements in the outer core as a function of time $X(t)$ by assuming that no light components enter the solid as

$$X(t) = \frac{X_0 M_C}{M_{OC}(t)}, \tag{20}$$

and the mass of the outer core is subsequently calculated as

$$M_{OC}(t) = 4\pi \int_{r_{IC}(t)}^{r_{OC}} \rho(x) x^2 dx = \frac{4}{3}\pi\rho_0 L_\rho^3 \left[f_C\left(\frac{r_{OC}}{L_\rho}\right) - f_C\left(\frac{r_{IC}(t)}{L_\rho}\right)\right]. \tag{21}$$

Therefore, if an inner core starts forming, the fraction of light elements in the outer core as a function of time will increase accordingly. As the outer core becomes gradually enriched in light elements, its composition shifts toward the eutectic point in the phase diagram. In the case of a binary core composition, the melting point depression by light elements corresponding to the attainment of the eutectic point can be as low as 200 K (Fe-Si at 65 GPa and Fe-O at 50 GPa; Kuwayama & Hirose [2004]; Seagle et al. [2008]) or 1500 K (Fe-S at 65 GPa; Morard, Andrault, et al. (2008)). Similar to what proposed in Morard, Bouchet, et al. (2011), we limit the melting point depression by light impurities to a maximum $\Delta T_{melt,\,core} = 1500$ K. This means that as soon as the melting point depression exerted by the presence of light components becomes higher than this threshold, the light element abundance in the outer core is anchored to a pressure-dependent "eutectic" value, for which the temperature reduction is exactly $\Delta T_{melt,\,core} = 1500$ K. During the subsequent evolution stages, the light element content in the outer core still increases, albeit less strongly, due to the varying ICB pressure. An additional effect that rises upon reaching the eutectic is that the compositions of the inner and outer core are equal, and the density jump at the ICB goes to zero. This effect is taken into account, as it can shut off magnetic activity if thermal buoyancy is not strong enough. We neglect density jumps associated with phase change.

2.4. Buoyancy Fluxes

Displacements of liquid in planetary cores result from both variations in their thermal and chemical structure. Thermally driven dynamos are generated by a superadiabatic heat flux at the CMB. Such a mechanism is thought to act predominantly during the early evolutionary stages of a planet when the core is very hot and releases a large amount of heat into the mantle (Del Genio et al., 2020). On the other hand, chemically-driven dynamos may start taking place later in time, once/if a solid inner core starts crystallizing. In this scenario, the density difference between the liquid and solid metal at the ICB resulting from the expulsion of light elements in the outer core can supply substantial energy to drive dynamo activity (Braginsky, 1963). Alternatively, snow mechanisms such as the rise of alloy-rich material (Braginsky, 1963), or the settling of solid iron through a stably stratified layer (Hauck et al., 2006; Rückriemen et al., 2018; Wong et al., 2018)

located in the immediate proximity of the ICB could provide an alternative source of buoyancy for core convection.

Here, we consider both contributions from thermal and chemical anomalies. As a result, the buoyancy flux is expressed as the sum of the thermal and the chemical buoyancy fluxes F_T and F_X. Following Driscoll and Bercovici (2014) we calculate these as

$$F_T = \frac{\alpha g}{\rho C_P} q_{c,conv} \tag{22}$$

$$F_X = \frac{g_{ICB} \Delta\rho_{ICB}}{\rho} \left(\frac{r_{IC}}{r_{OC}} \right)^2 \frac{dr_{IC}}{dt}, \tag{23}$$

where α is the thermal expansion coefficient, r_{IC} is the inner core radius, and $q_{c,conv} = q_{CMB} - q_{c,ad}$ is the convective heat flux at the CMB, defined as the difference between CMB and adiabatic heat flux. g_{ICB} is the gravity at the ICB and dr_{IC}/dt is the inner core growth rate. $\Delta\rho_{ICB}$ is the density jump at the ICB and is calculated using the relation $\Delta\rho_{ICB} = (\Delta\rho_{ICB,Earth}/X_{Earth})X_{planet}$, with $\Delta\rho_{ICB,\,Earth} = 600$ kg.m^{-3} the density jump at Earth's ICB and $X_{Earth} = 11\%$ is an estimate of Earth's light element content according to the melting temperature used in this study for which the main core component (iron) constitutes 89% of the core. Earth's density jump at the ICB has been determined with two types of seismic data, namely short-period body waves ($\Delta\rho_{ICB} \sim 520$–$1100$ kg.m^{-3}; Koper & Pyle [2004]; Tkalčić et al. [2009]) and long-period normal modes ($\Delta\rho_{ICB} \sim 820 \pm 180$ kg.m^{-3}; Masters & Gubbins [2003]). There is large uncertainty in the estimates resulting from differences in the resolution and accuracy of the sampling techniques and data processing. Before an inner core starts forming (and/or in the absence of light components), only temperature changes contribute to buoyancy.

The adiabatic heat flux is defined as

$$q_{c,ad} = k_c T_{CMB} r_{OC} \,/\, D_{ad}^2, \tag{24}$$

where k_c is the thermal conductivity of the core and T_{CMB} is the temperature at the CMB, which lies on the adiabat. The thermal conductivity determines how fast heat is conducted through the core into the mantle. Estimates for the thermal conductivity of Earth's core span values between ~ 20 Wm^{-1}K^{-1} (Konôpková et al., 2016) and ~ 160 Wm^{-1}K^{-1} (Gomi et al., 2013), with dramatic implications for the lifetime of the magnetic field (Labrosse, 2015). The uncertainties for Earth and the difficulty for experiments to attain the pressure range of the cores of massive rocky planets make it difficult to constrain thermal conductivities. Here, we use a constant thermal conductivity k_c of 150 Wm^{-1}K^{-1} (lying in the upper range of Earth's values) to obtain conservative estimates for the magnetic field lifetimes. In the Discussion (Section 4.4), we present how our results vary when employing different thermal conductivities (50 Wm^{-1}K^{-1} and 250 Wm^{-1}K^{-1}). We do not consider variations of thermal conductivity with pressure, temperature, and core composition (i.e., light element content). In general, thermal conductivity is thought to increase with increasing pressure. As a result, the thermal conductivities of massive planets could reach higher values, potentially leading to shorter magnetic field lifetimes than the ones calculated here. Similarly, the magnetic field lifetimes of small planets may be underestimated in the present study. D_{ad} is an adiabatic length scale (Labrosse et al., 2001) and amounts to $D_{ad} \sim 6{,}000$ km for Earth (Labrosse, 2003). We calculate D_{ad} for a given planet as $D_{ad} = \sqrt{3C_P \,/\, 2\pi\alpha_0\rho_0 G}$, where α_0 is the thermal expansion coefficient at the planetary center.

2.5. Magnetic Field

We calculate the magnetic moment m of a given rocky planet by using the scaling law proposed by Olson and Christensen (2006) as

$$m \simeq 4\pi r_{OC}^3 \beta \left(\rho \,/\, \mu_0 \right)^{1/2} ((F_T + F_X)(r_{OC} - r_{IC}))^{1/3}, \tag{25}$$

where β is a saturation constant for fast rotating dynamos ($\beta = 0.2$), $\mu_0 = 4\pi \cdot 10^{-7}$ Hm^{-1} is the magnetic permeability. Here, $r_{OC} - r_{IC}$ is the thickness of the convective shell in the core (i.e., the thickness of the liquid outer core). This quantity is obtained from the core evolution model and becomes smaller during inner core growth. The thermal and chemical buoyancy fluxes F_T and F_X are calculated from the core evolution model as well (Section 2.4). The magnetic field intensity at the CMB is calculated following Olson and Christensen (2006) as

$$B_{CMB} = \beta\left(\rho\mu_0\right)^{1/2}((F_T + F_X)(r_{OC} - r_{IC}))^{1/3}. \quad (26)$$

The intensity at the planetary surface B_{surf} scales from B_{CMB} as $B_{surf} = B_{CMB}(r_{OC} / r_{planet})^3$ (where r_{planet} is the planetary radius).

Equation 25 assumes that the magnetic field is dipolar, though we discuss the implications of core growth on different magnetic field morphologies in Section 4.1. Furthermore, this expression is devised for magnetic fields powered by convection in a liquid outer core, although it has recently been suggested that dynamos of super-Earths may also be generated in their mantles (Soubiran & Militzer, 2018), where iron-bearing minerals gain metallic properties. This process is not considered in the present study.

For a self-sustaining dynamo action to be viable, the magnetic Reynolds number $R_m = v(r_{OC} - r_{IC})/\eta_m$, where v is the flow velocity and η_m is the magnetic diffusivity (2 m^2s^{-1}; Jones & Schubert [2015]), needs to be higher than a critical value $R_{m,\,crit} = 40$, as suggested by numerical dynamo simulations (Christensen & Aubert, 2006; Roberts, 2015). The velocity of the convective flow v in the outer core is calculated using the scaling relation by Olson and Christensen (2006)

$$v \simeq 1.3((r_{OC} - r_{IC}) / \Omega)^{1/5}(F_T + F_X)^{2/5}, \quad (27)$$

where Ω is the rotation rate, which is assumed for simplicity to be the one of Earth ($\Omega = 7.29 \cdot 10^{-5}$ $rad.s^{-1}$). All cases addressed in this study feature super-critical conditions for dynamo action at the beginning of the evolution, as well as a high magnetic Reynolds number. A magnetic field shuts off if the inner core reaches the outer core radius, if the convective velocity v is too low, or if the CMB heat flow is lower than the heat conducted along the adiabat in the absence of inner core growth (chemical dynamos may be viable otherwise). We define the dynamo lifetime as the time interval in a planet's history during which the magnetic moment is non-zero. For the lifetime calculations, we consider the longest time interval of magnetic activity and do not consider subsequent sporadic field reactivations.

3. Results

3.1. Initial Core Structures

Hereafter, we present the core structures at the end of accretion, after the crystallization of the silicates at the CMB. These are calculated using the model CHIC (see also Section 2.1. Figure 2 shows internal structures (solid inner core, liquid outer core, silicate mantle) for planets of different mass and iron content (bulk and mantle) in the aftermath of accretion. The size of the solid inner core corresponds to the radius at which the temperature matches the core melting temperature (Equation 2), calculated for a given pressure and light element content. It can be seen that planets with higher bulk and mantle iron inventories feature large solid inner cores that can even reach up to the CMB radius. Large inner cores are a result of the increased internal pressures and densities of iron-rich planets, which raise the core melting temperature (Equation 2). Note that even though inner (and outer) core sizes increase for larger bulk iron inventories, planetary radii are smaller because of the higher core mass fraction (see Figure 2).

Figure 3 shows the inner core radius fraction (r_{IC}/r_{OC}) at the end of accretion for a larger range of explored parameters. Plots are shown for cores made of pure iron (left column) and for cores containing iron and 5% of light elements (right column). The upper and lower rows comprise cases with mantle iron numbers $\#Fe_M$ of 0 and 0.1, respectively. Internal structures for mantle iron numbers $\#Fe_M$ of 0.2 are shown in Figure S2, together with core structures after 5 Gyr of evolution for all masses and iron contents. We find that planets with cores made of pure iron and a mantle iron number of 0 (upper left panel in Figure 3) do not feature

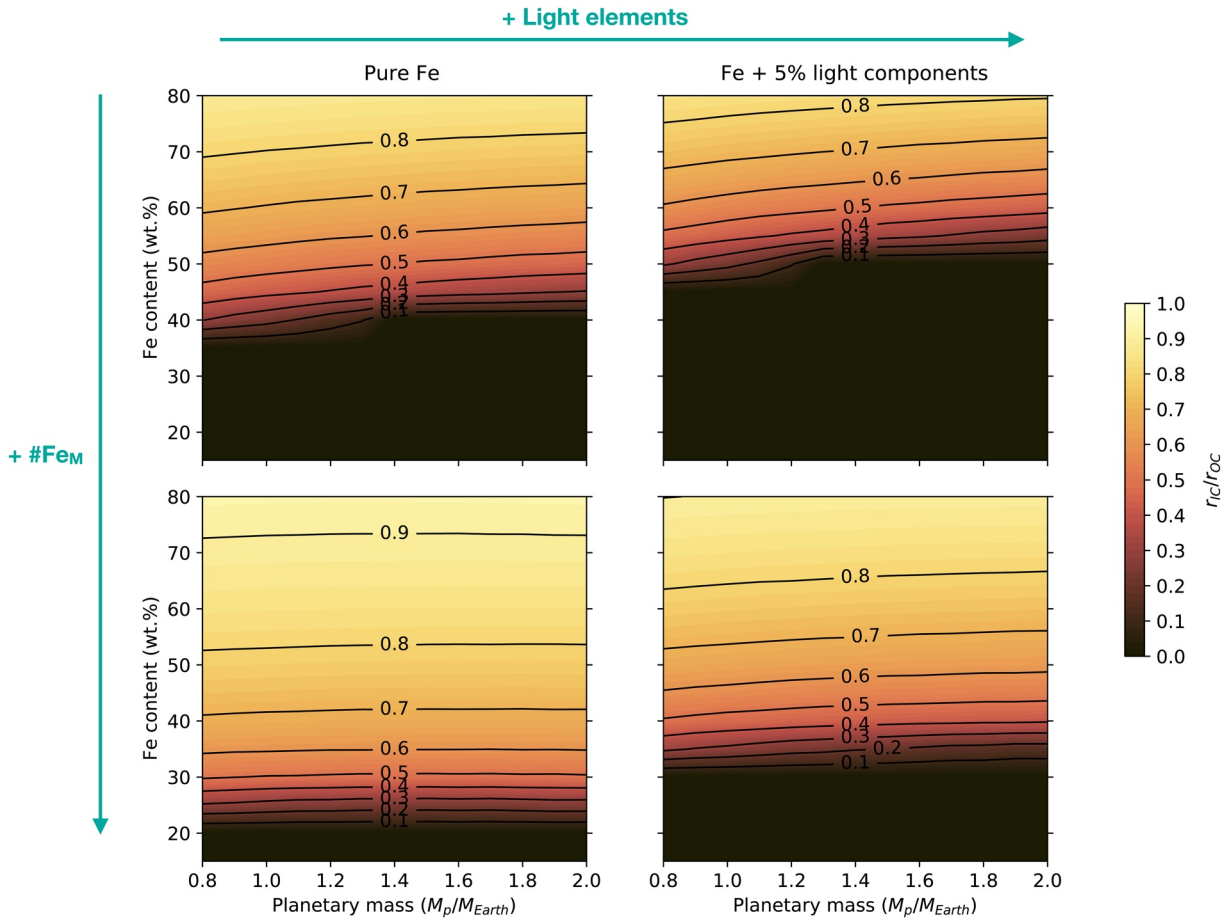

Figure 3. Inner core radius fraction (r_{IC}/r_{OC}) at the end of accretion as a function of planetary mass, bulk iron content, mantle iron number (upper row: $\#Fe_M = 0$, lower row: $\#Fe_M = 0.1$), and core composition (left column: pure iron, right column: iron and 5% light elements).

solid inner cores if the bulk iron content is smaller than $X_{Fe} \sim$ 35–40 wt.%, regardless of the planetary mass. Above this threshold, early inner cores are present and can reach up to > 80% of the core radius. The addition of 5% of light elements (Figure 3; right column) depresses the core melting temperature (see also Figure 1) and pushes the presence of a solid inner core to higher bulk iron contents. A different distribution of iron between core and mantle (i.e., a different mantle iron number) influences the inner core size as well. Planets with higher mantle iron numbers feature smaller core sizes, but solid inner cores tend to occupy a larger volume (see Figures 2 and 3). This is a result of the depression of the mantle liquidus, which in turn leads to lower temperatures at the CMB and at the planetary center (see Figure 1). In general, we find that partially solid cores are common for rocky planets in the aftermath of accretion, similar to the recent findings of Boujibar et al. (2020). We also find that core adiabats meet the melting temperature at the center, preventing the formation of a stably stratified layer and iron snow (Gaidos et al., 2010). Furthermore, we note that the inner core fractions do not seem to be strongly dependent on the planetary mass. Instead, the iron inventory, the distribution of iron between core and mantle, and the light element content are the main controlling parameters.

3.2. Core Evolution

Starting from planetary interior structures in the aftermath of accretion (see Sections 2.1 and 3.1), we investigate the evolution of the core using a parameterized thermal and magnetic evolution model (Section 2.2). Hereafter, we present some core evolution results for planets with masses of 1 and 2 M_{Earth} and bulk iron contents of 30 and 60 wt.% (see Figure 4). The core is made of iron and 5% light elements, and the mantle

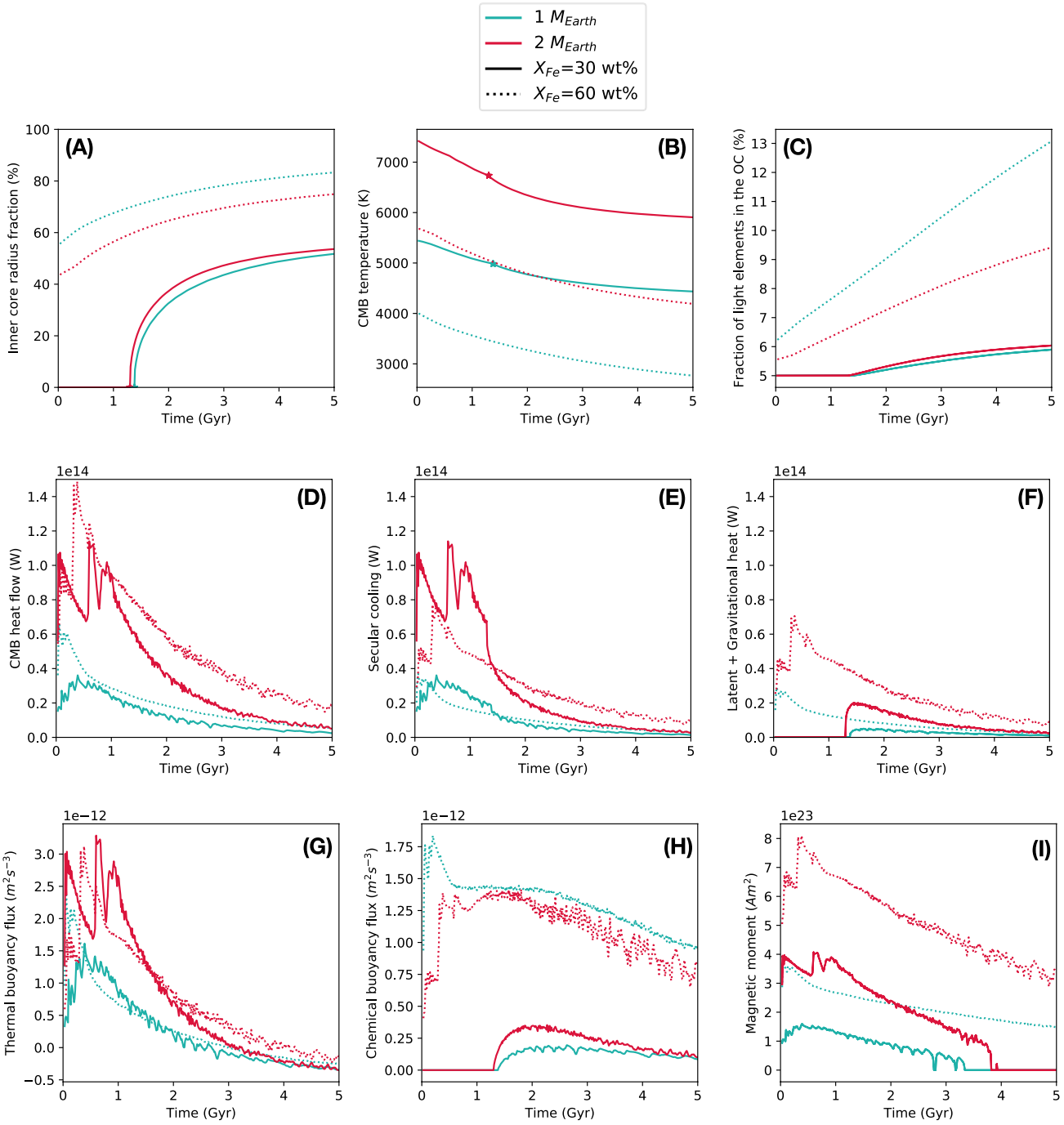

Figure 4. Evolution of the core during 5 Gyr for planets of 1 and 2 M_{Earth} with a bulk iron content of 30 and 60 wt.% and a mantle iron number $\#Fe_M$ of 0. The core is made of iron and 5% of light elements. The different panels show: (a) Inner core radius fraction. (b) CMB temperature. The stars mark the inner core crystallization onset. (c) Light element fraction in the liquid outer core (OC). (d) CMB heat flow for a stagnant-lid mantle. (e) Energy released from secular cooling. (f) Energy released from latent heat and gravitational heat. (g) Thermal buoyancy flux. (h) Chemical buoyancy flux. (i) Magnetic moment. As a reference, Earth's present-day magnetic moment is $7.8 \cdot 10^{22}$ Am^2. CMB, core-mantle boundary.

iron number $\#Fe_M$ is zero. General trends summarizing the outcomes of more simulations are shown in Section 3.3.

Inner core growth

Figures 4a and 4b show the growth of the inner core during 5 Gyr and the temperature evolution at the CMB, respectively, for planets of 1 and 2 M_{Earth} with different iron contents (30 wt.% and 60 wt.%) and $\#Fe_M = 0$ (for a core made of iron and 5% of light elements). In contrast to iron-rich bodies, planets with a reduced bulk iron content (30 wt.% in Figure 4) have smaller core mass fractions (see also Figures 2 and 3) and tend to feature fully liquid cores in the aftermath of accretion. As soon as the temperature at the planetary center reaches the melting temperature (after $\sim$ 1.5 Gyr in Figure 4a), an inner core starts growing as $r_{IC}(t) \propto \sqrt{t}$ (Labrosse, 2003, 2015). In this scenario, the inner core growth curve is steeper in the early crystallization stages due to the faster cooling of the planet and flattens out later on. Planets with a higher bulk iron content, on the other hand, tend to start out with partially solid cores (e.g., $\sim$ 45–55% solid core radius fractions for planets with 60 wt.% Fe in Figure 4). This is a result of the melting temperature slope flattening out at higher pressures, as shown in Figure 1. For all cases shown in Figure 4a, the solid inner core does not reach the outer core radius at the end of evolution, even though a large number of the analyzed bodies end up with fully solid cores after 5 Gyr (see also Section 3.3).

The temperature at the CMB lies on the adiabatic profile. Before an inner core starts crystallizing, the profile is anchored to the central temperature, which then shifts to the ICB temperature once an inner core starts forming (marked by a star in Figures 4a and 4b). The ICB temperature is assumed to be equal to the crystallization temperature of the core at the pressure of the ICB. As a result, the CMB temperature is higher for planets that start with no solid inner cores.

Light elements in the outer core As the solid inner core crystallizes, the volume of the liquid outer core shrinks and becomes gradually enriched with light impurities, as shown in Figure 4c. We assume that these impurities are preferentially partitioned into the liquid phase. In the scenarios explored in Figure 4, the core has a bulk fraction of light elements of 5%. However, depending on the initial size of the solid inner core, the initial light element content in the outer core will be different. Following the examples shown in Figures 4, a 1 M_{Earth} planet containing 60 wt.% of iron starts out with an inner core radius fraction of $\sim$ 55% (Figure 4a) and $\sim$ 6.3% of light elements in the outer core (Figure 4c). In contrast, a body of the same mass but containing 30 wt.% of iron features 5% of impurities in its fully liquid core. Due to the smaller inner core mass fraction of iron-poor bodies, the light element content in the liquid outer core will increase only by about $\sim$ 0.5% during evolution. On the other hand, bodies containing 60 wt.% of iron can grow large inner cores reaching up to $\sim$ 80% of the core radius, featuring thin liquid core shells containing more than 10% of light components. The light element content in the liquid portion of the core has strong implications for its chemical composition with respect to the eutectic and the presence of different core formation mechanisms, as will be pointed out in the Discussion (Section 4.2).

3.2.1. Energy Budget

Figure 4d shows the evolution of the contributions to the energy budget corresponding to the CMB heat flow histories for stagnant lid planets calculated using CHIC (see Section 2.1.4 and Noack et al. [2017]). In the absence of an inner core (and thus of chemical buoyancy), the CMB heat flow needs to be higher than the adiabatic one for thermal dynamo action to be viable. The crystallization of an inner core marks the onset of a chemical dynamo. In the absence of heat supplied by radioactive decay, before an inner core starts forming, the only energy contribution to the CMB heat flow is provided by the secular cooling term as shown in Figure 4e (see also Section 2.2). Once an inner core starts crystallizing, latent heat and gravitational energy (Figure 4f) start contributing to the energy balance, albeit being around one order of magnitude smaller than secular cooling.

More massive planets display higher CMB heat flows, resulting in higher secular cooling, latent, and gravitational heat terms. Despite having similar evolutions, the CMB heat flow curves are all characterized by sharp oscillations during the first $\sim$ 1 Gyr. Such fluctuations result from the initially very hot interior, triggering large-scale convective overturn not unsimilar to those seen in magma ocean crystallization studies (Ballmer et al., 2017; Maurice et al., 2017). At later evolution stages, CMB heat flows partially converge to becoming smoother, although oscillations are still possible due to small-scale convection.

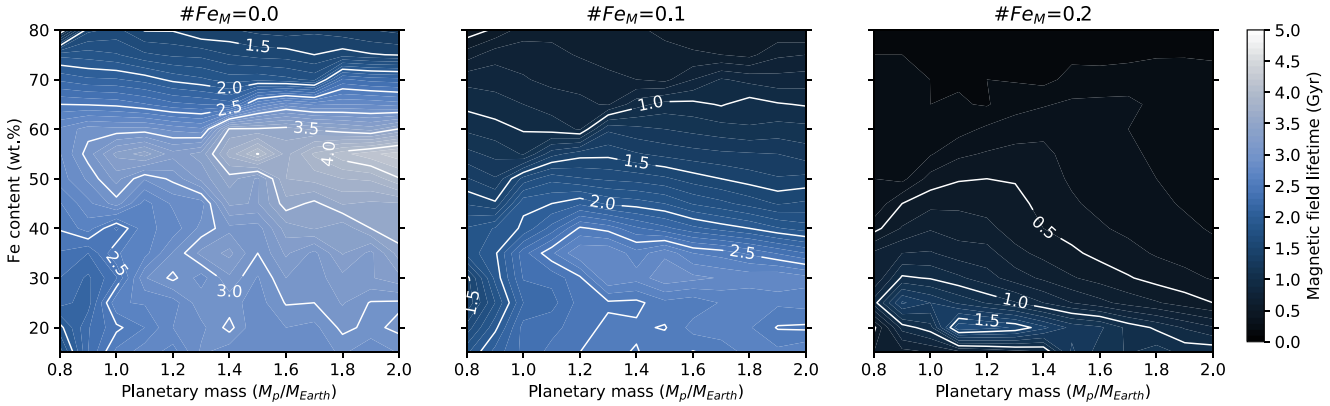

Figure 5. Magnetic field lifetimes for planets with different masses and bulk iron contents. Each panel comprises bodies with a different mantle iron number ($\#Fe_M = 0 - 0.2$). The core is made of pure iron.

3.2.2. Buoyancy Fluxes in the Outer Core

The evolution of the buoyancy fluxes arising from thermal and chemical anomalies is shown in panels G and H of Figure 4, respectively. As a planet cools, thermally-generated buoyancy decreases. The spikes in the thermal buoyancy flux curve reproduce the ones observed in the evolution of the CMB heat flow, as thermal buoyancy is proportional to the amount of heat extracted by the mantle from the core.

Chemical buoyancy is driven by the release of light elements into the outer core during inner core crystallization. The extent of chemical buoyancy is determined by the density jump at the ICB $\Delta\rho_{\mathrm{ICB}}$, which depends on the fraction of light elements present in the liquid outer core. As the outer core gradually becomes enriched in light components due to inner core crystallization, the density jump at the ICB increases accordingly. Nevertheless, chemical buoyancy decreases with time as a result of the smaller inner core growth rate (dr_{IC}/dt, see Equation 23) and drops to zero once the eutectic composition is reached.

3.2.3. Magnetic Field

The dipolar magnetic moment is calculated using the scaling law in Equation 25. Its evolution is shown in Figure 4i. As outlined in Section 2.5, magnetic activity can take place if the magnetic Reynolds number is higher than a critical value of 40 and if the core is not entirely solid. Furthermore, the magnetic field shuts off if the CMB heat flow is smaller than the conductive heat flow, even though the existence of chemical dynamos is made possible by inner core growth. We find that magnetic activity lasts longer (with lifetimes reaching up to more than $\sim$ 5 Gyr) for massive iron-rich planets due to their higher CMB heat flows and buoyancy fluxes. On the other hand, planets that are more iron-poor (e.g., 30 wt.%; see in Figure 4) tend to have shorter-lived magnetic fields, with lifetimes of $\sim$ 2.8 Gyr and $\sim$ 3.8 Gyr for 1 and 2 M_{Earth} planets, respectively. While an increased iron content extends the persistence of a magnetic field as shown in Figure 4i, we will show in the next section that too high bulk and mantle iron inventories can reduce the dynamo lifetime. After the magnetic field shuts off, there may be some sporadic field reactivation episodes (see Figure 4i for planets containing 30 wt.% of iron), resulting from the oscillatory behavior of the CMB heat flow and the thermal and chemical buoyancy fluxes. These episodes are not taken into account when calculating the magnetic field lifetimes.

3.3. Magnetic Field Lifetimes and Strengths

Hereafter, we present results exploring the full range of parameters introduced in this study. We focus on the evolution of the magnetic field, represented by its lifetime and maximum strength at the planetary surface. Results are shown as regime diagrams, with linear interpolations between the explored simulation cases.

Figure 5 shows the magnetic field lifetimes obtained for planets with different masses and iron contents (bulk and mantle) for cores made of pure iron. We find that the planetary iron content and distribution significantly influence the lifetime of the magnetic field. More specifically, we find that for each planetary

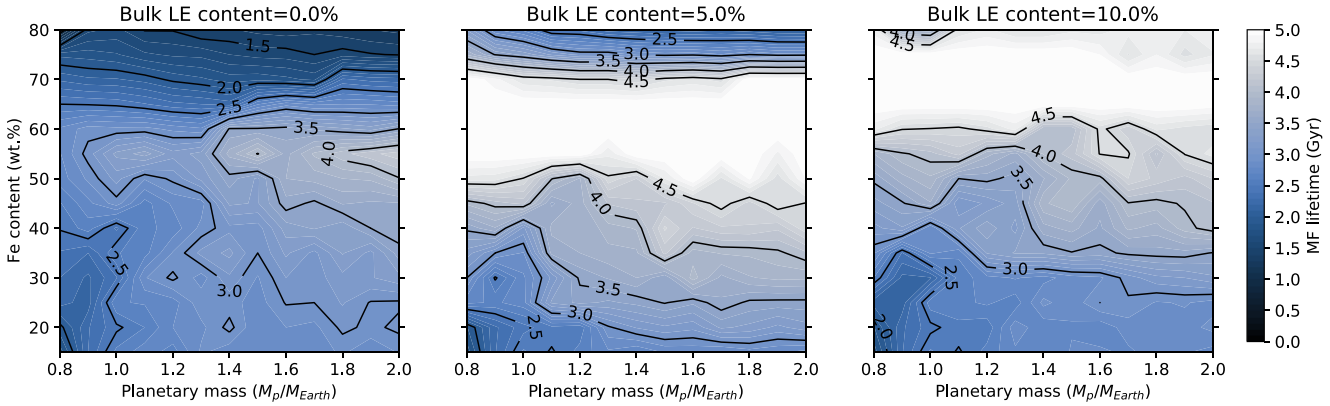

Figure 6. Magnetic field lifetimes for planets with different masses and bulk iron contents. The core is made of pure iron (left panel), as well as iron and light elements (middle and right panels). The mantle iron number is $\#Fe_M = 0$. The white regions indicate parameter combinations for which the magnetic field is still active at the end of the simulations (i.e., after 5 Gyr; see colorbar).

mass, the magnetic field lifetimes tend to increase up to intermediate bulk iron contents (~ 55 wt.% Fe), beyond which they start becoming shorter again. Since solid inner cores of iron-rich planets occupy larger core fractions (>50%) at the beginning of evolution (i.e., in the aftermath of accretion), magnetic activity tends to last shorter compared to iron-poor bodies. Similarly, an increase in the mantle iron inventory strongly shortens the period during which magnetic activity takes place. As a result, the longest dynamo lifetime estimates are ~ 4.25 Gyr, ~ 2.7 Gyr, and ~ 1.5 Gyr for planets with mantle iron numbers $\#Fe_M$ of 0, 0.1, and 0.2, respectively. This gradual shortening of the magnetic field lifetime with increasing mantle iron contents is again a result of the large inner core sizes arising from the depression of the mantle melting temperature (Figure 1). Rocky planets that are both very rich in iron and/or have large mantle iron fractions are thus likely to develop completely solid inner cores and to have no active magnetic field after 5 Gyr (see also Figures S2 and S3 for internal structures after 5 Gyr).

This scenario changes if the core contains a fraction of light elements. The lower melting temperatures caused by the presence of these light impurities lead to smaller or absent solid inner cores. As a result, the longest magnetic field lifetimes (>5 Gyr) are shifted toward higher bulk iron inventories (Figure 6). For bodies with large amounts of light elements (e.g., 10%), inner core crystallization could be delayed to a point in time at which the CMB heat flow is subadiabatic and chemical buoyancy is not strong enough to counter this effect, leading to the extinction of the field before an inner core starts forming. In general, we find that most bodies are able to sustain magnetic activity at least once during their evolution. The magnetic field lifetime is mainly limited by the full solidification of the core and by the CMB heat flow dropping below the conductive heat flow.

Figure 7 shows the temporal maximum dipole field intensity at the planetary surface (i.e., the maximum field strength over 5 Gyr), obtained for planets with different masses and iron contents for cores made of pure iron. Following the relation in Equation 26, the magnetic field strength is smaller for large planets having small core mass fractions. This quantity is also proportional to the heat flow at the CMB (which influences thermal buoyancy fluxes) and is therefore expected to be highest during the early stages of a planet's evolution (see Figures4D 4d and 4I). The surface intensity is important to assess the detectability of the generated magnetic fields (see Section 4.5). We obtain the highest surface field intensities (~ 160 μT, around five times stronger than the one at present-day for Earth) for massive planets with high bulk iron contents and low fractions of mantle iron. Therefore, despite displaying shorter-lived magnetic fields (Figure 5), iron-rich planets (>70 wt.% Fe) are expected to feature stronger magnetic fields during their early evolution. The addition of light components to the core increases chemical buoyancy fluxes and leads to thicker convective shells (i.e., smaller inner cores) and surface intensities of up to ~ 310 μT (Figure 8).

Figure 9 summarizes our results by showing the planetary masses and radii, calculated using the interior profiles in Noack and Lasbleis (2020), as well as the magnetic field lifetimes obtained with the core evolution model. These are shown for planets with different masses and mantle iron numbers $\#Fe_M$ having a

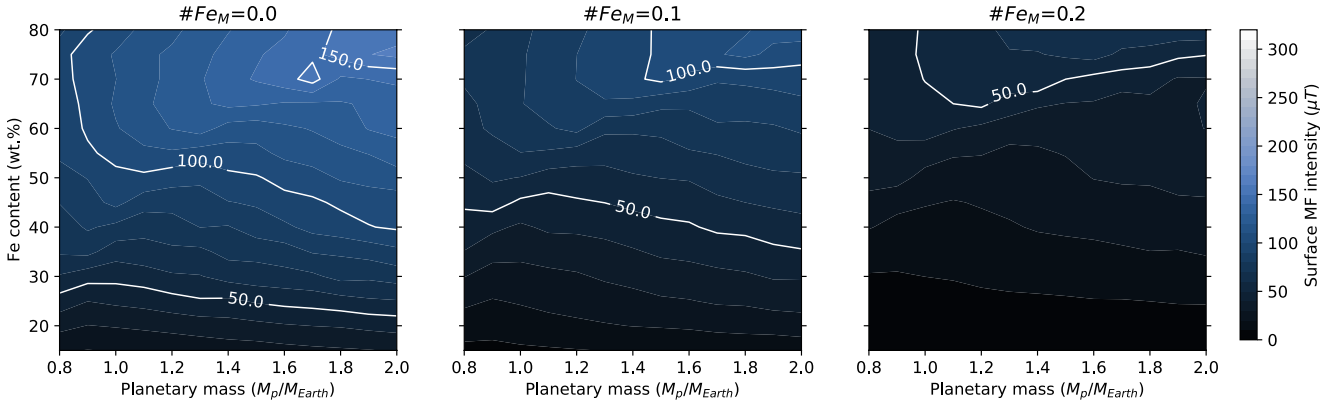

Figure 7. Temporal maximum magnetic field intensity at the planetary surface (as a reference, Earth's present-day surface intensity field is 30 μT). Each panel comprises bodies with a different mantle iron number. The core is made of pure iron.

core made of pure iron. Together with the planetary mass, the planetary radius is one of the observables for exoplanets and is used here as a proxy for the bulk iron content, with larger radii indicating a lower iron inventory. The content of Figure 9 is equivalent to what is presented in Figure 5, where longer magnetic field lifetimes are obtained for low mantle iron numbers and intermediate bulk iron contents (i.e., intermediate planetary radii). Our results indicate that both a planet's iron content and the distribution of iron between the mantle and the core (and the planetary mass, albeit to a lesser extent) have strong implications for the dynamo lifetime. This also confirms that the planetary mass and radius alone are insufficient for constraining exoplanetary internal structures, dynamics, and magnetic field features. Understanding the interaction of internallygenerated magnetic fields with the atmosphere will open new avenues for constraining interior properties starting from atmospheric observations.

4. Discussion

4.1. Implications of Large Inner Cores

During the course of their evolution, a large portion of the analyzed cores becomes fully or mostly solid. In the former case, the inner core has grown up to the size of the liquid outer core, whereas in the latter case the core consists of a large solid inner core and a thin convective shell. Besides having dramatic consequences for the existence of a magnetic field, this scenario can also have strong implications for the dynamo morphology and the pattern of convection in the remaining liquid. Figure 10 shows the time required for the solid inner core to reach 70% of the outer core radius, for planets of 1 and 2 M_{Earth} with different bulk and mantle iron contents (the core is made of pure iron). Since bodies with high mantle iron numbers tend

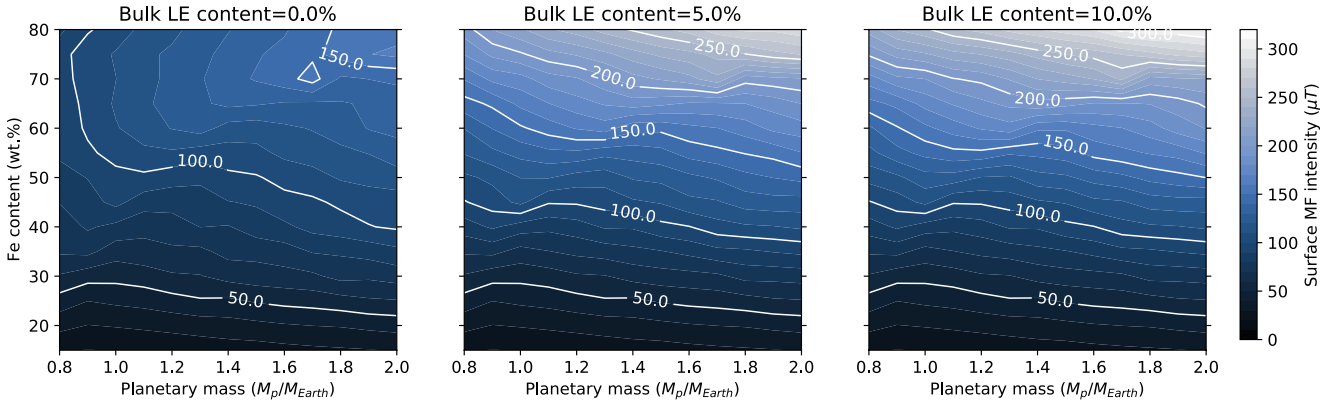

Figure 8. Temporal maximum magnetic field intensity at the planetary surface (as a reference, Earth's present-day surface intensity field is 30 μT). The mantle iron number Fe_{M} is 0. Each panel comprises bodies with a different light element content.

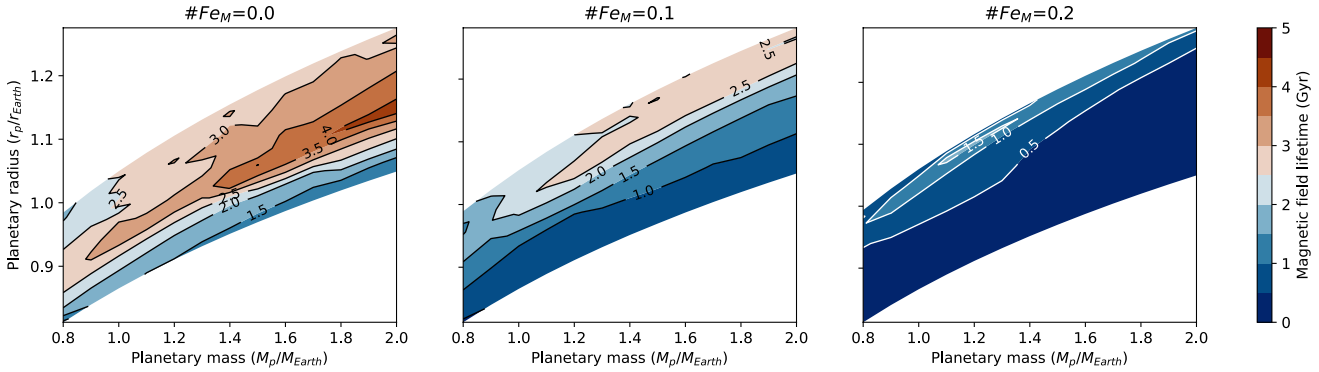

Figure 9. Magnetic field lifetimes obtained for planets with different masses, bulk iron contents, and mantle iron numbers $\#Fe_M$. The core is made of pure iron. The planetary radii are calculated using the profiles in Noack and Lasbleis (2020). *Note.* that the different mantle iron numbers in the three panels lead to different planetary radii.

to start their evolution with larger inner cores, the time elapsed until the outer core radius is reached is substantially reduced. As a result, 1 M_{Earth} planet having a bulk iron content of 15 wt.% and a mantle iron number $\#Fe_M = 0$ requires more than 5 Gyr for its core to become 70% solid, whereas it takes only ~ 2.7 Gyr for the same planet with a mantle iron number of 0.2. This is even more extreme for 2 M_{Earth} planets, for which the time is reduced to less than 1 Gyr for a mantle iron number of 0.2. The time required to reach a solid core fraction of 70% can be extended by adding light core impurities.

Several studies have investigated dynamo morphology at different inner core fractions. Heimpel et al. (2005) examined the power spectra for dynamos at different shell geometries. They showed that for inner core fractions lying between $r_{IC}/r_{OC} = 0.15$–0.65, the dipole energy increases up to $r_{IC}/r_{OC} = 0.45$. Above this threshold, it slowly decays while the octupolar and quadrupolar contributions gradually increase. The importance of non-dipolar components has also been found by Takahashi and Matsushima (2006), who investigated convection in a thin shell with the inner core occupying 70% of the core radius. Based on similar findings, Stanley et al. (2007) suggested that a high octupole contribution might hint at the presence of a large inner core, whereas dipolar configurations might be a signature of small (Earth-like) solid inner cores. A change in the magnetic field morphology can affect its potential detectability, with high-order configurations remaining more concentrated in the planetary interior and not manifesting at the surface.

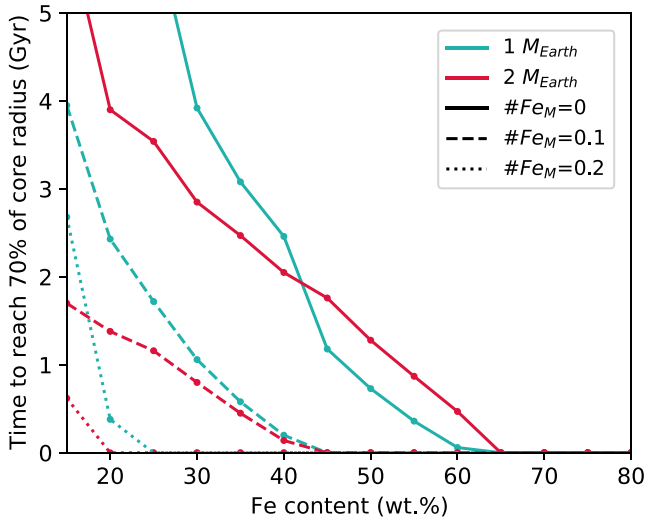

Figure 10. Time required for the solid inner core to reach 70% of the core radius as a function of bulk iron content, for planets with 1 and 2 M_{Earth} and different mantle iron numbers $\#Fe_M$. The core is made of pure iron. For planets with low iron contents (bulk and mantle) the inner core does not reach 70% of the core radius during 5 Gyr of evolution.

Large inner cores can also influence the dynamics in the remaining thin liquid shell. The Rayleigh number Ra is related to the shell thickness D_{shell} as $Ra \propto D_{\text{shell}}^3$. Following this, the presence of a thin liquid outer core volume leads to a smaller Rayleigh number (while keeping similar buoyancy fluxes), and hence to less vigorous convection. The resulting convective pattern, taking place in a region with a wide aspect ratio of horizontal and vertical scales of convection, might be described by a different set of equations than those used here. A thin liquid layer can also affect flows powering the magnetic field. For cases with a small or absent inner core, magnetic activity is powered by large-scale columnar flows acting over the whole volume of the liquid outer core. In the presence of a thin shell, these columnar flows might shift to smaller scales, which in turn might alter the strength and the long-term stability of the magnetic field.

While a large inner core might influence the dynamo configuration and outer core dynamics to a certain extent, it is still unclear at which inner core fraction this starts happening and thus requires further investigation. We note that once inner cores become very large in our models, the equations employed here might not adequately describe the dynamics at that stage.

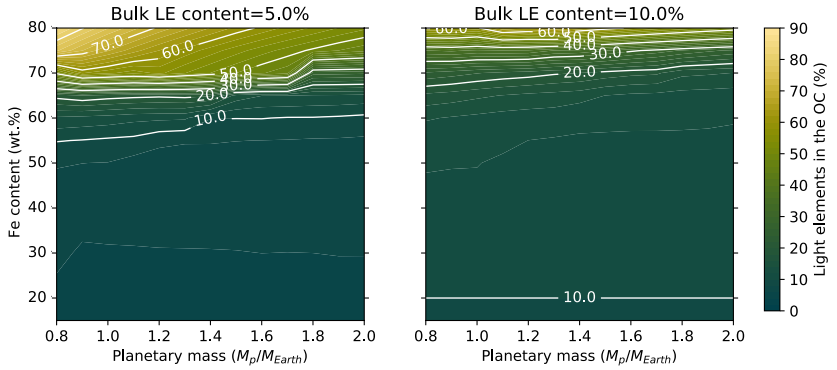

Figure 11. Fraction of light elements (LE) in the liquid outer core (OC) after 5 Gyr of evolution as a function of planetary mass and bulk iron content. The left and right panels show results for cores starting with bulk light element contents of 5% and 10%. We assume that light components strongly partition into the liquid phase. The iron number $\#Fe_M$ is 0 for all cases.

4.2. Composition of the Outer Core

As the inner core grows, the density and the composition of the outer core change due to the addition of light elements expelled from the inner core. Here, we assume that light components strongly partition into the liquid phase. The abundance of light impurities in exoplanetary cores is unconstrained, mainly due to their high pressures, which are challenging for mineral physics experiments and ab initio studies to reproduce. In our simulations, we consider cores with bulk light element abundances of up to 10%. However, in the presence of large solid inner cores, light element fractions in the liquid outer core can be substantially higher. Figure 11 shows light element abundances in the outer core after 5 Gyr of evolution for 5% and 10% bulk light element fractions for planets of different mass and bulk iron content. Planets with a smaller light element inventory (i.e., 5%) tend to grow larger (and older) solid inner cores than planets with larger inventories of light elements. As a result, the outer core becomes more enriched in light components compared to bodies with larger bulk amounts of light elements (i.e., 10%), with fractions reaching up to $X \sim 90\%$.

At such high light element contents, the outer core composition might lie at or beyond the eutectic point, on the iron-poor side of the phase diagram. This would result in core crystallization taking place on an alloy-rich liquidus, as well as the potential occurrence of different processes responsible for core crystallization, such as iron snow. These mechanisms may modify the energy balance in ways that are beyond the scope of the present study. Furthermore, such a process may more likely occur for planets larger than 2 M_{Earth} (Gaidos et al., 2010). In an attempt to simulate the attainment of the eutectic point, we topped the melting temperature depression to a maximum value of $\Delta T_{\text{melt, core}} = 1500$ K, as proposed by Morard et al. (2011), beyond which outer core composition is kept to a pressure-dependent "eutectic" value and $\Delta\rho_{\text{ICB}} = 0$ (even though the density jump is likely non-zero due to phase change). While our approach somewhat simulates the core reaching a eutectic, it should be noted that eutectic compositions for alloys at conditions similar to the ones of super-Earths' interiors require further investigation.

4.3. Influence of the Initial Thermal Profiles

The CMB heat flow histories employed here are calculated using the code CHIC (Noack et al., 2017) for planets in a stagnant lid tectonic configuration. The presence of a single stagnant ductile lithospheric plate acts as a cap and reduces the amount of heat that is released at the planetary surface. As a result, the CMB heat flows employed here will be lower than for bodies featuring mobile lid-like mechanisms, which cool down at a faster rate. A similar effect might be exerted by the presence of an overlying thick atmosphere (Lopez & Fortney, 2014; Weiss & Marcy, 2014), which maintains the planetary interior hot. The use of CMB heat flows for stagnant lid planets does not reproduce the thermal and magnetic history of Earth's core. Nevertheless, our core evolution model is based on the one by Labrosse (2015), and using a similar CMB heat flow history to the one employed there would lead to an evolution equivalent to Earth.

A further underestimation of the CMB heat flow arises from not taking into account the input of latent and gravitational heat released from the growth of an inner core. Better coupling between mantle and core evolution is thus needed. However, for this study, we employ a hot initial thermal profile, which is an upper limit of the profile in Stixrude (2014). In this scenario, the CMB temperature is anchored to the mantle liquidus, leading to an initially hot core. This may promote higher CMB heat flows than those obtained in previous work (Tackley et al., 2013; Valencia et al., 2006).

In order to compare our results with other thermal profiles, we ran the evolution models for bodies with a warm initial temperature profile, which corresponds to the profile described in Stixrude (2014) and to the "warm" case in Noack and Lasbleis (2020). In this scenario, the temperature at the CMB is anchored to the mantle solidus. Hot and warm initial thermal profiles can represent different stages in a planet's evolution, as well as a different thickness of the overlying atmosphere if any (Hamano et al., 2013). In this regard, a hot profile would be indicative of a planet surrounded by a thick insulating atmosphere, which would delay mantle freezing and lead to a long-lived magma ocean. On the other hand, a warm initial profile would represent a planet featuring a thinner atmosphere.

The results of the warm start runs are shown in Figures S4 and S5. Starting from a warm internal profile implies lower CMB heat flows and cores that are partially or entirely solid. We find that regardless of the iron content (bulk and mantle), cores made of pure iron end up completely solid after 5 Gyr. As a result, the magnetic field lifetime is drastically reduced and reaches a maximum value of $\sim$ 2.8 Gyr for low bulk iron contents (<20 wt.%) and mantle iron numbers ($\#Fe_M = 0$). The longest magnetic field lifetimes are shifted to lower bulk iron contents compared to the hot cases (55 wt.%; Figure 5), which is a consequence of the larger initial solid core fractions. Similar to the hot start scenarios, the presence of light impurities can help to maintain the field for up to $\sim$ 5 Gyr or longer. Again, this upper estimate is obtained for cores having bulk iron contents of 30–60 wt.%, somewhat lower than for the hot start cases (Figure 6).

4.4. Influence of the Thermal Conductivity of the Core

The lifetime of a magnetic field is also highly dependent on the thermal conductivity of the core, which determines the rate at which heat is conducted to the mantle. A number of recent findings reporting higher core thermal conductivities than previously thought (Gomi et al., 2013; Pozzo et al., 2012) have dramatically challenged the current understanding of processes taking place in the cores of Earth and other planets. Other processes enabling a longer-lived dynamo action for Earth matching paleomagnetic observations have since then been invoked (Hirose et al., 2017; O'Rourke & Stevenson, 2016).

Thermal conductivity varies as a function of pressure, temperature, and composition (i.e., light element content). The value of the thermal conductivity of Earth's core is highly debated ($\sim$ 20 $Wm^{-1}K^{-1}$; Konôpková et al. [2016] $\sim$ 160 $Wm^{-1}K^{-1}$; Gomi et al. [2013]). The high uncertainties for Earth make it even more difficult to predict thermal conductivity values for super-Earths' cores. For this reason, for the work presented here, we decided to employ a constant thermal conductivity of $\sim$ 150 $Wm^{-1}K^{-1}$, lying in the upper range of estimates for Earth. However, thermal conductivity is thought to increase with planetary mass ($k \approx k_{\mathrm{Earth}}(M / M_{\mathrm{Earth}})^{(1/2)}$, where k_{Earth} is the thermal conductivity of Earth's core, M is the planetary mass, and M_{Earth} is Earth's mass; Stixrude (2014)). This may lead to shorter magnetic field lifetimes for high planetary masses than those calculated here. Similarly, the pressure-independent conductivity employed here may lead to an underestimation of the magnetic field lifetimes of smaller planets. The light element inventory in the core also influences the thermal conductivity, which is not explored here. Future work will need to address the dependence of the thermal conductivity on different planetary parameters to provide more accurate estimates for dynamo lifetimes.

As a comparison, we vary this parameter down to 50 $Wm^{-1}K^{-1}$ and up to 250 $Wm^{-1}K^{-1}$ to show the variation in the calculated magnetic field lifetimes. The results are shown in the Supplementary Information (Figures S6 and S7). For cores made of pure iron, we obtain upper estimates of the magnetic field lifetime amounting to more than 5 Gyr for planets with thermal conductivity of 50, and almost 2 Gyr lower (3.3 Gyr) for bodies having a thermal conductivity of 250 $W.m^{-1}.K^{-1}$. Similar to the cases for thermal conductivity of 150 $Wm^{-1}K^{-1}$, the longest lifetimes are obtained for mantle iron numbers of 0 and for intermediate bulk

iron contents (i.e., 55 wt.%). The addition of light elements extends the magnetic field lifetimes to up to longer than 5 Gyr for both thermal conductivities.

4.5. Detectability

Magnetic fields of planets in the solar system were first detected from the ground by measuring the radio electron cyclotron emission generated from the interaction between the stellar wind and the magnetized planet. These observations were carried out using radio telescopes, similar to the Low-Frequency Array (LOFAR, Kassim et al. [2004]). Only signals with frequencies greater than 10 MHz (i.e., the ionospheric cutoff) are able to penetrate Earth's atmosphere and be detected by such telescopes. This constitutes a bias on the type of magnetic fields that can be observed, which are mainly those produced by giant planets.

In order to be detectable, the magnetic field of a planet must fulfill two conditions: it must produce cyclotron emission signals with frequencies higher than the ionospheric cutoff of 10 MHz (and thus have a magnetic field surface intensity of $B_s = 384\ \mu$T) and have a flux density higher than the sensitivity of the instrument the observation is carried out with. The sensitivity describes the minimum signal that a telescope is able to detect within a given time interval. The flux density is related to a planet's distance from the solar system, its cyclotron frequency, and its radio emission. The latter quantity depends on a planet's magnetic moment and its orbital distance. Planets located in systems further away from the Sun will thus need to be located at smaller orbital distances in order to be detected.

In their study, Driscoll and Olson (2011) have discussed the potential observability of exoplanetary magnetic fields through radio emissions using the LOFAR radio telescope, and we redirect the reader to that paper for more information on the relevant equations. We find that all planets modeled here emit at frequencies lower than the ionospheric cutoff, with the maximum surface field strength $B_s = 311\ \mu$T (Figure 8) corresponding to a cyclotron frequency of ~ 8 MHz. While this signal cannot enter the Earth's atmosphere, the planetary radio emission can be affected by the stellar activity, which influences the intensity, density, and velocity of stellar winds. For example, sporadic energetic events such as coronal mass ejections can increase the flux density of the signal by $1 - 2$ orders of magnitude (Farrell et al., 1999), and planets located further away from the host star may become temporarily detectable. While the emission generated by rocky exoplanets' magnetic fields is challenging to be detected by current ground instrumentation, space-based observations and the development of indirect observation techniques (Fossati et al., 2010; Withers & Vogt, 2017) can provide valuable insights on planetary composition, interior structure, and magnetic activity.

5. Summary and Conclusions

The presence of a magnetic field during a planet's history is thought to influence its evolution and the development and long-term stability of habitable surface conditions. Magnetic fields of rocky bodies are generated in an electrically conductive liquid layer in their deep interior (the metallic molten outer core for Earth). The discovery of a large number of exoplanets and the search for extraterrestrial life motivates the investigation of the evolution and diversity of exodynamos. This constitutes a challenging task, as the interior properties of exoplanets are difficult to estimate from current data.

This work presents structures and evolution trends for the cores of a diverse set of planets with different masses ($0.8 - 2\ M_{\text{Earth}}$), bulk iron contents (indicated by the bulk iron fraction), as well as variable partitioning of iron between the mantle and the core (indicated by the mantle iron number). We employ an interior structure model (Noack et al., 2017) to obtain core structures at the late stages of planet formation. Starting from these, we model the thermal and magnetic evolution of the core and calculate if and how long magnetic activity is sustained. Our main findings are:

- While the planetary mass is not a highly controlling parameter, the iron inventory strongly affects a planet's core structure, as well as its thermal and magnetic evolution.
- In agreement with the recent findings by Boujibar et al. (2020), we find that the presence of a partially solid core is common among newly formed planets. Larger solid cores are obtained for planets with high bulk and/or high mantle iron contents due to the higher core mass fraction and the lower mantle

melting temperature. Cores containing small fractions of light elements start out with smaller solid fractions due to the depression of the core melting temperature exerted by light impurities.

- Most modeled planets can sustain thermally and/or chemically driven dynamo activity during 5 Gyr of evolution. For pure iron cores, the generated magnetic fields can remain active for up to $\sim$ 4.25 Gyr, where longer lifetimes are obtained for planets with intermediate iron fractions (55 wt.%) and low mantle iron numbers. Dynamo lifetimes can be extended to 5 Gyr or longer in the presence of a small fraction of core impurities. The duration of magnetic activity is mainly limited by the growth of the solid inner core up to the CMB radius (occurring for iron-rich planets with high mantle iron contents) and by the CMB heat flow falling below the adiabatic heat flow.
- After 5 Gyr, a large portion of the analyzed cores become mostly or fully solid. Solid inner cores occupying more than $\sim$ 70% of the volume of the core may be compatible with lower dipole energy and different convection patterns, compared to cases with a smaller inner solid sphere. This may affect the generation and detectability of a magnetic field.
- Inner core growth leads to the gradual expulsion of light impurities into the liquid outer core, resulting in light element fractions reaching up to $\sim$ 90% after 5 Gyr of evolution. Large light element contents may lead to the attainment of a core composition at or beyond the eutectic. This may lead to core crystallization mechanisms powering the magnetic field in a different way, not explored in this study.
- Surface magnetic field intensities of planets with core impurities can reach up to $\sim$ 310 μT, about 10 times the one of present-day Earth. For these strengths, the frequency and the emitted flux are too weak to be detected by current ground-based radio telescopes. The use of indirect observation strategies will provide further constraints on exoplanetary magnetism.

Investigating the diversity of exoplanetary magnetic fields will improve our understanding of the evolution of planets in our solar system and beyond. Ultimately, it is important to constrain the influence and feedback of internally generated magnetic fields on the planetary atmospheric evolution and habitability by fully coupling interior processes to ones taking place in the atmosphere and the stellar environment. This will enable us to constrain interior properties from future observed atmospheric parameters. This study provides the first step in this direction by presenting some trends obtained from the evolution of exoplanetary cores.

Data Availability Statement

The simulations were analyzed using the open-source software environment Matplotlib (Hunter, 2007). Figures were generated using the perceptually uniform scientific color maps lajolla, oslo, and bamako (Crameri, 2018) to prevent visual distortion. All codes and notebooks needed to reproduce the figures in the paper are available at Bonati and Lasbleis (April 27, 2021).

Acknowledgments
This research has made use of the Exoplanet Orbit Database and the Exoplanet Data Explorer at exoplanets.org. IB acknowledges financial support from the Japanese Society for the Promotion of Science (JSPS). ML was funded by the European Union's Horizon 2020 research and innovation program under the Marie Skłodowska-Curie Grant Agreement No. 795289. LN acknowledges financial support from the German Research Foundation (DFG) for project NO 1324/6-1. IB and ML thank Guillaume Morard, John Hernlund, and Hagay Amit for helpful discussions. The authors appreciate the support of ELSI, Tokyo, to host the Planetary Diversity Workshop in 2016, which initiated this study. LN would like to thank the HPC Service of ZEDAT, Freie Universität Berlin, for computing time. The authors thank two anonymous reviewers for their constructive comments, which considerably improved the manuscript and Laurent Montési for the editorial handling.

References

Abe, Y. (1997). Thermal and chemical evolution of the terrestrial magma ocean. *Physics of the Earth and Planetary Interiors*, *100*(1–4), 27–39. https://doi.org/10.1016/s0031-9201(96)03229-3

Akeson, R. L., Chen, X., Ciardi, D., Crane, M., Good, J., Harbut, M., et al. (2013). The NASA exoplanet archive: data and tools for exoplanet research. *Publications of the Astronomical Society of the Pacific*, *125*(930), 989. https://doi.org/10.1086/672273

Andrault, D., Bolfan-Casanova, N., Nigro, G. L., Bouhifd, M. A., Garbarino, G., & Mezouar, M. (2011). Solidus and liquidus profiles of chondritic mantle: Implication for melting of the earth across its history. *Earth and Planetary Science Letters*, *304*(1–2), 251–259. https://doi.org/10.1016/j.epsl.2011.02.006

Aubert, J., Labrosse, S. p., & Poitou, C. (2009). Modeling the palaeo-evolution of the geodynamo. *Geophysical Journal International*, *179*(3), 1414–1428. https://doi.org/10.1111/j.1365-246x.2009.04361.x

Badro, J., Brodholt, J. P., Piet, H., Siebert, J., & Ryerson, F. J. (2015). Core formation and core composition from coupled geochemical and geophysical constraints. *Proceedings of the National Academy of Sciences of the United States of America*, *112*(40), 12310–12314. https://doi.org/10.1073/pnas.1505672112

Ballmer, M. D., Lourenço, D. L., Hirose, K., Caracas, R., & Nomura, R. (2017). Reconciling magma-ocean crystallization models with the present-day structure of the Earth's mantle. *Geochemistry, Geophysics, Geosystems*, *18*(7), 2785–2806. https://doi.org/10.1002/2017gc006917

Baraffe, I., Chabrier, G., Fortney, J., & Sotin, C. (2014). *Planetary internal structures*. arXiv preprint arXiv:1401.4738.

Bitsch, B., & Battistini, C. (2020). Influence of sub- and super-solar metallicities on the composition of solid planetary building blocks. *Astronomy & Astrophysics*, *633*, A10. https://doi.org/10.1051/0004-6361/201936463

Blanchard, I., Siebert, J., Borensztajn, S., & Badro, J. (2017). The solubility of heat-producing elements in Earth's core. *Geochemical Perspective Letters*, *5*, 1–5. https://doi.org/10.7185/geochemlet.1737

Bonati, I., & Lasbleis, M. (2021, April 27). *Marinelasbleis/coreevolution: v1.0.1 (Version v1.0.1). Zenodo*. http://doi.org/10.5281/zenodo.4723640

Bond, J. C., O'Brien, D. P., & Lauretta, D. S. (2010). The compositional diversity of extrasolar terrestrial planets. i. in situ simulations. *Acta Pathologica Japonica*, *715*(2), 1050. https://doi.org/10.1088/0004-637x/715/2/1050
Bouchet, J., Mazevet, S., Morard, G., Guyot, F., & Musella, R. (2013). Ab initio equation of state of iron up to 1500 gpa. *Physical Review B*, *87*(9), 094102. https://doi.org/10.1103/physrevb.87.094102
Boujibar, A., Driscoll, P., & Fei, Y. (2020). Super-earth internal structures and initial thermal states. *Journal of Geophysical Research: Planets*, *125*(5), e2019JE006124. https://doi.org/10.1029/2019je006124
Boukaré, C. E., Ricard, Y., & Fiquet, G. (2015). Thermodynamics of the MgO-FeO-SiO 2 system up to 140 GPa: Application to the crystallization of Earth's magma ocean. *Journal of Geophysical Research: Solid Earth*, *120*(9), 6085–6101. https://doi.org/10.1002/2015jb011929
Braginsky, S. (1963). Structure of the f layer and reasons for convection in the earth's core. *Soviet Physics Doklady*, *149*, 8–10.
Braginsky, S., & Roberts, P. H. (1995). Equations governing convection in earth's core and the geodynamo. *Geophysical & Astrophysical Fluid Dynamics*, *79*(1–4), 1–97. https://doi.org/10.1080/03091929508228992
Brain, D., Leblanc, F., Luhmann, J., Moore, T. E., & Tian, F. (2013). *Planetary magnetic fields and climate evolution* (p. 487). cctp.
Breuer, D., Labrosse, S., & Spohn, T. (2010). Thermal evolution and magnetic field generation in terrestrial planets and satellites. *Space Science Reviews*, *152*(1–4), 449–500. https://doi.org/10.1007/s11214-009-9587-5
Buffett, B. A. (2003). Geophysics: The thermal state of Earth's core. *Science*, *299*(5613), 1675–1677. https://doi.org/10.1126/science.1081518
Canup, R. M. (2004). Dynamics of lunar formation. *Annual Review of Astronomy and Astrophysics*, *42*, 441–475. https://doi.org/10.1146/annurev.astro.41.082201.113457
Chidester, B. A., Rahman, Z., Righter, K., & Campbell, A. J. (2017). Metal-silicate partitioning of U: Implications for the heat budget of the core and evidence for reduced U in the mantle. *Geochimica et Cosmochimica Acta*, *199*, 1–12. https://doi.org/10.1016/j.gca.2016.11.035
Christensen, U. R., & Aubert, J. (2006). Scaling properties of convection-driven dynamos in rotating spherical shells and application to planetary magnetic fields. *Geophysical Journal International*, *166*(1), 97–114. https://doi.org/10.1111/j.1365-246x.2006.03009.x
Cohen, Z., McWilliams, R. S., Gómez-Pérez, N., & Goncharov, A. F. (2016). Direct measurement of thermal conductivity in solid iron at planetary core conditions. *Nature*, *534*(7605), 99–101. https://doi.org/10.1038/nature18009
Crameri, F. (2018). Scientific color-maps. *Zenodo*, *10*. https://doi.org/10.5281/zenodo.3596401
Dehant, V., Lammer, H., Kulikov, Y. N., Grießmeier, J.-M., Breuer, D., Verhoeven, O., et al. (2007). Planetary magnetic dynamo effect on atmospheric protection of early earth and mars. *Space Science Reviews*, *129*(1–3), 279–300. https://doi.org/10.1007/s11214-007-9163-9
Dorn, C., Harrison, J. H. D., Bonsor, A., & Hands, T. O. (2019). A new class of super-earths formed from high-temperature condensates: Hd219134 b, 55 cnc e, wasp-47 e. *Monthly Notices of the Royal Astronomical Society*, *484*(1), 712–727. https://doi.org/10.1093/mnras/sty3435
Dorn, C., Noack, L., & Rozel, A. B. (2018). Outgassing on stagnant-lid super-earths. *Astronomy & Astrophysics*, *614*, A18. https://doi.org/10.1051/0004-6361/201731513
Driscoll, P., & Bercovici, D. (2014). On the thermal and magnetic histories of earth and venus: Influences of melting, radioactivity, and conductivity. *Physics of the Earth and Planetary Interiors*, *236*, 36–51. https://doi.org/10.1016/j.pepi.2014.08.004
Driscoll, P., & Olson, P. (2011). Optimal dynamos in the cores of terrestrial exoplanets: Magnetic field generation and detectability. *Icarus*, *213*(1), 12–23. https://doi.org/10.1016/j.icarus.2011.02.010
Dumoulin, C., Tobie, G., Verhoeven, O., Rosenblatt, P., & Rambaux, N. (2017). Tidal constraints on the interior of venus. *Journal of Geophysical Research: Planets*, *122*(6), 1338–1352. https://doi.org/10.1002/2016je005249
Elkins-Tanton, L. T., & Seager, S. (2008). Coreless terrestrial exoplanets. *The Astrophysical Journal*, *688*(1), 628.
Farrell, W. M., Desch, M. D., & Zarka, P. (1999). On the possibility of coherent cyclotron emission from extrasolar planets. *Journal of Geophysical Research*, *104*(E6), 14025–14032. https://doi.org/10.1029/1998je900050
Fossati, L., Haswell, C. A., Froning, C. S., Hebb, L., Holmes, S., Kolb, U., et al. (2010). Metals in the exosphere of the highly irradiated planet wasp-12b. *Acta Pathologica Japonica*, *714*(2), L222. https://doi.org/10.1088/2041-8205/714/2/l222
Fraeman, A. A., & Korenaga, J. (2010). The influence of mantle melting on the evolution of mars. *Icarus*, *210*(1), 43–57. https://doi.org/10.1016/j.icarus.2010.06.030
Frank, E. A., Meyer, B. S., & Mojzsis, S. J. (2014). A radiogenic heating evolution model for cosmochemically earth-like exoplanets. *Icarus*, *243*, 274–286. https://doi.org/10.1016/j.icarus.2014.08.031
Fu, S., Yang, J., Zhang, Y., Liu, J., Greenberg, E., Prakapenka, V. B., et al. (2018). Melting behavior of the lower-mantle ferropericlase across the spin crossover: Implication for the ultra-low velocity zones at the lowermost mantle. *Earth and Planetary Science Letters*, *503*, 1–9. https://doi.org/10.1016/j.epsl.2018.09.014
Gardner, J. P., Mather, J. C., Clampin, M., Doyon, R., Greenhouse, M. A., Hammel, H. B., et al. (2006). The james webb space telescope. *Space Science Reviews*, *123*(4), 485–606. https://doi.org/10.1007/s11214-006-8315-7
Gomi, H., Ohta, K., Hirose, K., Labrosse, S., Caracas, R., Verstraete, M. J., & Hernlund, J. W. (2013). The high conductivity of iron and thermal evolution of the Earth's core. *Physics of the Earth and Planetary Interiors*, *224*, 88–103. https://doi.org/10.1016/j.pepi.2013.07.010
Gubbins, D. (1977). Energetics of the earth's core. *Journal of Geophysics-Zeitschrift f r Geophysik*, *43*(1), 453–464.
Hakim, K., Rivoldini, A., Van Hoolst, T., Cottenier, S., Jaeken, J., Chust, T., & Steinle-Neumann, G. (2018). A new ab initio equation of state of hcp-fe and its implication on the interior structure and mass-radius relations of rocky super-earths. *Icarus*, *313*, 61–78. https://doi.org/10.1016/j.icarus.2018.05.005
Hamano, K., Abe, Y., & Genda, H. (2013). Emergence of two types of terrestrial planet on solidification of magma ocean. *Nature*, *497*(7451), 607–610. https://doi.org/10.1038/nature12163
Hauck, S. A., Aurnou, J. M., & Dombard, A. J. (2006). Sulfur's impact on core evolution and magnetic field generation on ganymede. *Journal of Geophysical Research: Planets*, *111*(E9). https://doi.org/10.1029/2005je002557
Heimpel, M., Aurnou, J., Al-Shamali, F., & Perez, N. G. (2005). A numerical study of dynamo action as a function of spherical shell geometry. *Earth and Planetary Science Letters*, *236*(1–2), 542–557. https://doi.org/10.1016/j.epsl.2005.04.032
Hernlund, J. W., & Tackley, P. J. (2008). Modeling mantle convection in the spherical annulus. *Physics of the Earth and Planetary Interiors*, *171*(1–4), 48–54. https://doi.org/10.1016/j.pepi.2008.07.037
Hirose, K., Labrosse, S., & Hernlund, J. (2013). Composition and state of the core. *Annual Review of Earth and Planetary Sciences*, *41*, 657–691. https://doi.org/10.1146/annurev-earth-050212-124007
Hirose, K., Morard, G., Sinmyo, R., Umemoto, K., Hernlund, J., Helffrich, G., & Labrosse, S. (2017). Crystallization of silicon dioxide and compositional evolution of the Earth's core. *Nature*, *543*(7643), 99–102. https://doi.org/10.1038/nature21367
Howe, A. R., Burrows, A., & Verne, W. (2014). Mass-radius relations and core-envelope decompositions of super-earths and sub-neptunes. *Acta Pathologica Japonica*, *787*(2), 173. https://doi.org/10.1088/0004-637x/787/2/173

Huguet, L., Van Orman, J. A., Hauck, S. A., II, & Willard, M. A. (2018). Earth's inner core nucleation paradox. *Earth and Planetary Science Letters*, *487*, 9–20. https://doi.org/10.1016/j.epsl.2018.01.018

Hunter, J. D. (2007). Matplotlib: A 2d graphics environment. *Computer Science and Engineering*, *9*(3), 90–95. https://doi.org/10.1109/MCSE.2007.55

Ishii, E., Nagata, Y., Suzuki, A., & Kato, T. (1995). Melting relations of peridotite and the density crossover in planetary mantles. *Chemical Geology*, *120*(3–4), 207–221. https://doi.org/10.1016/0009-2541(94)00139-y

Jones, C., & Schubert, G. (2015). Thermal and compositional convection in the outer core. *Treatise in Geophysics, Core Dynamics*, *8*, 131–185.

Karatekin, A. D., Brain, D., Noack, L., & Schaefer, L. (2020). The inner solar system's habitability through time. *Planetary Astrobiology*, *419*.

Karato, S.-i., & Wu, P. (1993). Rheology of the upper mantle: A synthesis. *Science*, *260*(5109), 771–778. https://doi.org/10.1126/science.260.5109.771

Kassim, N. E., Lazio, T. J. W., Ray, P. S., Crane, P. C., Hicks, B. C., Stewart, K. P., et al. (2004). The low-frequency array (lofar): Opening a new window on the universe. *Planetary and Space Science*, *52*(15), 1343–1349. https://doi.org/10.1016/j.pss.2004.09.013

Konopliv, A. S., & Yoder, C. F. (1996). Venusiank2tidal Love number from Magellan and PVO tracking data. *Geophysical Research Letters*, *23*(14), 1857–1860. https://doi.org/10.1029/96gl01589

Koper, K. D., & Pyle, M. L. (2004). Observations of pkikp/pcp amplitude ratios and implications for earth structure at the boundaries of the liquid core. *Journal of Geophysical Research: Solid Earth*, *109*(B3). https://doi.org/10.1029/2003jb002750

Kuchner, M. J., & Seager, S. (2005). *Extrasolar carbon planets*. arXiv preprint astro-ph/0504214.

Kuwayama, Y., & Hirose, K. (2004). Phase relations in the system fe-fesi at 21 gpa. *American Mineralogist*, *89*(2–3), 273–276. https://doi.org/10.2138/am-2004-2-303

Labrosse, S. (2003). Thermal and magnetic evolution of the earth's core. *Physics of the Earth and Planetary Interiors*, *140*(1–3), 127–143. https://doi.org/10.1016/j.pepi.2003.07.006

Labrosse, S. (2015). Thermal evolution of the core with a high thermal conductivity. *Physics of the Earth and Planetary Interiors*, *247*, 36–55. https://doi.org/10.1016/j.pepi.2015.02.002

Labrosse, S., Hernlund, J. W., & Coltice, N. (2007). A crystallizing dense magma ocean at the base of the Earth's mantle. *Nature*, *450*(7171), 866–869. https://doi.org/10.1038/nature06355

Labrosse, S., Poirier, J.-P., & Le Mouël, J.-L. (2001). The age of the inner core. *Earth and Planetary Science Letters*, *190*(3–4), 111–123. https://doi.org/10.1016/s0012-821x(01)00387-9

Lammer, H., Zerkle, A. L., Gebauer, S., Tosi, N., Noack, L., & Scherf, M., et al. (2018). Origin and evolution of the atmospheres of early venus, earth and mars. *Astronomy and Astrophysics Review*, *26*(1), 2. https://doi.org/10.1007/s00159-018-0108-y

Lay, T., Hernlund, J., & Buffett, B. A. (2008). Core-mantle boundary heat flow. *Nature Geosciences*, *1*(1), 25. https://doi.org/10.1038/ngeo.2007.44

Lee, K. K., & Jeanloz, R. (2003). High-pressure alloying of potassium and iron: Radioactivity in the earth's core? *Geophysical Research Letters*, *30*(23). https://doi.org/10.1029/2003gl018515

Lister, J. R., & Buffett, B. A. (1995). The strength and efficiency of thermal and compositional convection in the geodynamo. *Physics of the Earth and Planetary Interiors*, *91*(1–3), 17–30. https://doi.org/10.1016/0031-9201(95)03042-u

Liu, H., Kennett, B. L., & Cormier, V. F. (2009). On the inner—outer core density contrast from pkikp/pcp amplitude ratios and uncertainties caused by seismic noise. *Geophysical Journal International*, *179*(1), 425–443.

Lopez, E. D., & Fortney, J. J. (2014). Understanding the mass-radius relation for sub-neptunes: Radius as a proxy for composition. *Acta Pathologica Japonica*, *792*(1), 1. https://doi.org/10.1088/0004-637x/792/1/1

López-Morales, M., Gómez-Pérez, N., & Ruedas, T. (2011). Magnetic fields in earth-like exoplanets and implications for habitability around m-dwarfs. *Origins of Life and Evolution of the Biosphere*, *41*(6), 533–537. https://doi.org/10.1007/s11084-012-9263-8

Lourenço, D. L., Rozel, A. B., Ballmer, M. D., & Tackley, P. J. (2020). Plutonic-squishy lid: A new global tectonic regime generated by intrusive magmatism on earth-like planets. *Geochemistry, Geophysics, Geosystems*, *21*(4), e2019GC008756. https://doi.org/10.1029/2019gc008756

Madhusudhan, N., Lee, K. K. M., & Mousis, O. (2012). A possible carbon-rich interior in super-earth 55 cancri e. *Acta Pathologica Japonica*, *759*(2), L40. https://doi.org/10.1088/2041-8205/759/2/l40

Masters, G., & Gubbins, D. (2003). On the resolution of density within the earth. *Physics of the Earth and Planetary Interiors*, *140*(1–3), 159–167. https://doi.org/10.1016/j.pepi.2003.07.008

Maurice, M., Tosi, N., Samuel, H., Plesa, A.-C., Hüttig, C., & Breuer, D. (2017). Onset of solid-state mantle convection and mixing during magma ocean solidification. *Journal of Geophysical Research: Planets*, *122*(3), 577–598. https://doi.org/10.1002/2016je005250

McDonough, W. F., & Sun, S.-S. (1995). The composition of the earth. *Chemical Geology*, *120*(3–4), 223–253. https://doi.org/10.1016/0009-2541(94)00140-4

McIntyre, S. R., Lineweaver, C. H., & Ireland, M. J. (2019). Planetary magnetism as a parameter in exoplanet habitability. *Monthly Notices of the Royal Astronomical Society*, *485*(3), 3999–4012.

Miozzi, F., Morard, G., Antonangeli, D., Clark, A. N., Mezouar, M., Dorn, C., et al. (2018). Equation of state of sic at extreme conditions: New insight into the interior of carbon-rich exoplanets. *Journal of Geophysical Research: Planets*, *123*(9), 2295–2309. https://doi.org/10.1029/2018je005582

Moore, T. E., & Horwitz, J. (2007). Stellar ablation of planetary atmospheres. *Reviews of Geophysics*, *45*(3). https://doi.org/10.1029/2005rg000194

Moore, W. B., & Webb, A. A. G. (2013). Heat-pipe earth. *Nature*, *501*(7468), 501–505. https://doi.org/10.1038/nature12473

Morard, G., Andrault, D., Guignot, N., Sanloup, C., Mezouar, M., Petitgirard, S., & Fiquet, G. (2008). In situ determination of fe–fe3s phase diagram and liquid structural properties up to 65 gpa. *Earth and Planetary Science Letters*, *272*(3–4), 620–626. https://doi.org/10.1016/j.epsl.2008.05.028

Morard, G., Bouchet, J., Valencia, D., Mazevet, S., & Guyot, F. (2011). The melting curve of iron at extreme pressures: Implications for planetary cores. *High Energy Density Physics*, *7*(3), 141–144. https://doi.org/10.1016/j.hedp.2011.02.001

Moriarty, J., Madhusudhan, N., & Fischer, D. (2014). Chemistry in an evolving protoplanetary disk: effects on terrestrial planet composition. *Acta Pathologica Japonica*, *787*(1), 81. https://doi.org/10.1088/0004-637x/787/1/81

Nakagawa, T., & Tackley, P. J. (2010). Influence of initial cmb temperature and other parameters on the thermal evolution of earth's core resulting from thermochemical spherical mantle convection. *Geochemistry, Geophysics, Geosystems*, *11*(6). https://doi.org/10.1029/2010gc003031

Nakagawa, T., & Tackley, P. J. (2013). Implications of high core thermal conductivity on Earth's coupled mantle and core evolution. *Geophysical Research Letters*, *40*(11), 2652–2656. https://doi.org/10.1002/grl.50574

Nakajima, M., & Stevenson, D. J. (2015). Melting and mixing states of the Earth's mantle after the Moon-forming impact. *Earth and Planetary Science Letters*, *427*, 286–295. https://doi.org/10.1016/j.epsl.2015.06.023
Nimmo, F. (2002). Why does venus lack a magnetic field? *Geology*, *30*(11), 987–990. https://doi.org/10.1130/0091-7613(2002)030<0987:wdvlam>2.0.co;2
Nimmo, F. (2007). Energetics of the core. *Treatise on Geophysics*, *8*, 31–65. https://doi.org/10.1016/b978-044452748-6.00128-0
Nimmo, F., Primack, J., Faber, S. M., Ramirez-Ruiz, E., & Safarzadeh, M. (2020). Radiogenic heating and its influence on rocky planet dynamos and habitability. *Acta Pathologica Japonica*, *903*(2), L37. https://doi.org/10.3847/2041-8213/abc251
Nimmo, F., & Schubert, G. (2015). *Treatise on geophysics*. Elsevier Amsterdam.
Noack, L., Godolt, M., von Paris, P., Plesa, A.-C., Stracke, B., Breuer, D., & Rauer, H. (2014). Can the interior structure influence the habitability of a rocky planet? *Planetary and Space Science*, *98*, 14–29. https://doi.org/10.1016/j.pss.2014.01.003
Noack, L., & Lasbleis, M. (2020). Parameterisations of interior properties of rocky planets: Investigation of planets with earth-like compositions but variable iron content. *Astronomy & Astrophysics*.
Noack, L., Rivoldini, A., & Van Hoolst, T. (2017). Volcanism and outgassing of stagnant-lid planets: implications for the habitable zone. *Physics of the Earth and Planetary Interiors*, *269*, 40–57. https://doi.org/10.1016/j.pepi.2017.05.010
Nomura, R., Ozawa, H., Tateno, S., Hirose, K., Hernlund, J., Muto, S., et al. (2011). Spin crossover and iron-rich silicate melt in the Earth's deep mantle. *Nature*, *473*(7346), 199–202. https://doi.org/10.1038/nature09940
Okuchi, E., Conrad, C. P., Manga, M., & Hernlund, J. (2010). Thermodynamic limits on magnetodynamos in rocky exoplanets. *Acta Pathologica Japonica*, *718*(2), 596. https://doi.org/10.1088/0004-637x/718/2/596
Olson, P., & Christensen, U. R. (2006). Dipole moment scaling for convection-driven planetary dynamos. *Earth and Planetary Science Letters*, *250*(3–4), 561–571. https://doi.org/10.1016/j.epsl.2006.08.008
Olson, P., Deguen, R., Hinnov, L. A., & Zhong, S. (2013). Controls on geomagnetic reversals and core evolution by mantle convection in the phanerozoic. *Physics of the Earth and Planetary Interiors*, *214*, 87–103. https://doi.org/10.1016/j.pepi.2012.10.003
O'Neill, C., Lenardic, A., Weller, M., Moresi, L., Quenette, S., & Zhang, S. (2016). A window for plate tectonics in terrestrial planet evolution? *Physics of the Earth and Planetary Interiors*, *255*, 80–92.
O'Rourke, J. G., & Stevenson, D. J. (2016). Powering earth's dynamo with magnesium precipitation from the core. *Nature*, *529*(7586), 387–389.
Poirier, J.-P. (1994). Light elements in the earth's outer core: A critical review. *Physics of the Earth and Planetary Interiors*, *85*(3–4), 319–337. https://doi.org/10.1016/0031-9201(94)90120-1
Pozzo, M., Davies, C., Gubbins, D., & Alfè, D. (2012). Thermal and electrical conductivity of iron at Earth's core conditions. *Nature*, *485*(7398), 355–358. https://doi.org/10.1038/nature11031
Roberts, P. (2015). Theory of the geodynamo. *Core Dynamics*, 67–105.
Rogers, L. A., & Seager, S. (2010). A framework for quantifying the degeneracies of exoplanet interior compositions. *Acta Pathologica Japonica*, *712*(2), 974. https://doi.org/10.1088/0004-637x/712/2/974
Rozel, J., Andrault, D., & Samuel, H. (2016). On the cooling of a deep terrestrial magma ocean. *Earth and Planetary Science Letters*, *448*, 140–149. https://doi.org/10.1016/j.epsl.2016.05.010
Rubie, D. C., Frost, D. J., Mann, U., Asahara, Y., Nimmo, F., Tsuno, K., et al. (2011). Heterogeneous accretion, composition and core–mantle differentiation of the earth. *Earth and Planetary Science Letters*, *301*(1–2), 31–42. https://doi.org/10.1016/j.epsl.2010.11.030
Rückriemen, T., Breuer, D., & Spohn, T. (2018). Top-down freezing in a Fe-FeS core and Ganymede's present-day magnetic field. *Icarus*, *307*, 172–196. https://doi.org/10.1016/j.icarus.2018.02.021
Safonova, M., Murthy, J., & Shchekinov, Y. A. (2016). Age aspects of habitability. *International Journal of Astrobiology*, *15*(2), 93–105. https://doi.org/10.1017/s1473550415000208
Schneider, J., Dedieu, C., Le Sidaner, P., Savalle, R., & Zolotukhin, I. (2011). Defining and cataloging exoplanets: the exoplanet.eu database. *Astronomy & Astrophysics*, *532*, A79. https://doi.org/10.1051/0004-6361/201116713
Schubert, G., & Soderlund, K. M. (2011). Planetary magnetic fields: Observations and models. *Physics of the Earth and Planetary Interiors*, *187*(3–4), 92–108. https://doi.org/10.1016/j.pepi.2011.05.013
Seager, S., Kuchner, M., Hier-Majumder, C. A., & Militzer, B. (2007). Mass-radius relationships for solid exoplanets. *Acta Pathologica Japonica*, *669*(2), 1279. https://doi.org/10.1086/521346
Seagle, C., Heinz, D., Campbell, A., Prakapenka, V., & Wanless, S. (2008). Melting and thermal expansion in the fe–feo system at high pressure. *Earth and Planetary Science Letters*, *265*(3–4), 655–665. https://doi.org/10.1016/j.epsl.2007.11.004
Soubiran, F., & Militzer, B. (2018). Electrical conductivity and magnetic dynamos in magma oceans of super-earths. *Nature Communications*, *9*(1), 1–7. https://doi.org/10.1038/s41467-018-06432-6
Spergel, D., Gehrels, N., Baltay, C., Bennett, D., Breckinridge, J., & Donahue, M., et al. (2015). *Wide-field infrarred survey telescope-astrophysics focused telescope assets wfirst-afta 2015 report*. arXiv preprint arXiv:1503.03757.
Spiegel, D. S., Fortney, J. J., & Sotin, C. (2014). Structure of exoplanets. *Proceedings of the National Academy of Sciences*, *111*(35), 12622–12627. https://doi.org/10.1073/pnas.1304206111
Stamenković, V., & Breuer, D. (2014). The tectonic mode of rocky planets: Part 1–driving factors, models & parameters. *Icarus*, *234*, 174–193.
Stamenković, V., Noack, L., Breuer, D., & Spohn, T. (2012). The influence of pressure-dependent viscosity on the thermal evolution of super-earths. *The Astrophysical Journal*, *748*(1), 41.
Stanley, S., Zuber, M., & Bloxham, J. (2007). Using reversed magnetic flux spots to determine a planet's inner core size. *Geophysical Research Letters*, *34*(19). https://doi.org/10.1029/2007gl030892
Stein, C., Schmalzl, J., & Hansen, U. (2004). The effect of rheological parameters on plate behavior in a self-consistent model of mantle convection. *Physics of the Earth and Planetary Interiors*, *142*(3–4), 225–255. https://doi.org/10.1016/j.pepi.2004.01.006
Stevenson, D. J., Spohn, T., & Schubert, G. (1983). Magnetism and thermal evolution of the terrestrial planets. *Icarus*, *54*(3), 466–489. https://doi.org/10.1016/0019-1035(83)90241-5
Stixrude, L. (2014). Melting in super-earths. *Philosophical Transactions of the Royal Society of A.*, *372*, 20130076. https://doi.org/10.1098/rsta.2013.0076
Stixrude, L., de Koker, N., Sun, N., Mookherjee, M., & Karki, B. B. (2009). Thermodynamics of silicate liquids in the deep earth. *Earth and Planetary Science Letters*, *278*(3–4), 226–232. https://doi.org/10.1016/j.epsl.2008.12.006
Stixrude, L., & Lithgow-Bertelloni, C. (2011). Thermodynamics of mantle minerals - II. Phase equilibria. *Geophysical Journal International*, *184*(3), 1180–1213. https://doi.org/10.1111/j.1365-246x.2010.04890.x
Strangeway, R., Russell, C., Luhmann, J., Moore, T., Foster, J., Barabash, S., & Nilsson, H. (2010). *Does a planetary-scale magnetic field enhance or inhibit ionospheric plasma outflows? AGUFM*.

Tachinami, C., Senshu, H., & Ida, S. (2010). Thermal evolution and lifetime of intrinsic magnetic fields of super-earths in habitable zones. *Acta Pathologica Japonica*, *726*(2), 70. https://doi.org/10.1088/0004-637x/726/2/70

Tackley, P. J., Ammann, M., Brodholt, J. P., Dobson, D. P., & Valencia, D. (2013). Mantle dynamics in super-earths: Post-perovskite rheology and self-regulation of viscosity. *Icarus*, *225*(1), 50–61. https://doi.org/10.1016/j.icarus.2013.03.013

Takahashi, F., & Matsushima, M. (2006). Dipolar and non-dipolar dynamos in a thin shell geometry with implications for the magnetic field of mercury. *Geophysical Research Letters*, *33*(10). https://doi.org/10.1029/2006gl025792

Tarduno, J. A., Cottrell, R. D., Watkeys, M. K., Hofmann, A., Doubrovine, P. V., Mamajek, E. E., et al. (2010). Geodynamo, solar wind, and magnetopause 3.4 to 3.45 billion years ago. *Science*, *327*(5970), 1238–1240. https://doi.org/10.1126/science.1183445

Tosi, N., Yuen, D. A., de Koker, N., & Wentzcovitch, R. M. (2013). Mantle dynamics with pressure- and temperature-dependent thermal expansivity and conductivity. *Physics of the Earth and Planetary Interiors*, *217*, 48–58. https://doi.org/10.1016/j.pepi.2013.02.004

Valencia, D., O'Connell, R. J., & Sasselov, D. (2006). Internal structure of massive terrestrial planets. *Icarus*, *181*(2), 545–554. https://doi.org/10.1016/j.icarus.2005.11.021

van Summeren, J., Gaidos, E., & Conrad, C. P. (2013). Magnetodynamo lifetimes for rocky, earth-mass exoplanets with contrasting mantle convection regimes. *Journal of Geophysical Research: Planets*, *118*(5), 938–951. https://doi.org/10.1002/jgre.20077

Weiss, L. M., & Marcy, G. W. (2014). The mass-radius relation for 65 exoplanets smaller than 4 earth radii. *Acta Pathologica Japonica*, *783*(1), L6. https://doi.org/10.1088/2041-8205/783/1/l6

Withers, P., & Vogt, M. F. (2017). *Occultations of astrophysical radio sources as probes of planetary environments: A case study of jupiter and possible applications to exoplanets*. arXiv preprint arXiv:1702.07075.

Wohlers, A., & Wood, B. J. (2017). Uranium, thorium and ree partitioning into sulfide liquids: Implications for reduced s-rich bodies. *Geochimica et Cosmochimica Acta*, *205*, 226–244. https://doi.org/10.1016/j.gca.2017.01.050

Wong, J., Davies, C. J., & Jones, C. A. (2018). A Boussinesq slurry model of the F-layer at the base of Earth's outer core. *Geophysical Journal International*, *214*(3), 2236–2249. https://doi.org/10.1093/gji/ggy245

Wood, B. J., Walter, M. J., & Wade, J. (2006). Accretion of the earth and segregation of its core. *Nature*, *441*(7095), 825–833. https://doi.org/10.1038/nature04763

Yamazaki, D., & Karato, S.-i. (2001). Some mineral physics constraints on the rheology and geothermal structure of Earth's lower mantle. *American Mineralogist*, *86*(4), 385–391. https://doi.org/10.2138/am-2001-0401

Zerr, A., & Boehler, R. (1993). Melting of (Mg, Fe) SiO_3 perovskite under hydrostatic, inert conditions to 580 kbar. *EOS Transactions of the American Geophysical Union*, *74*, 168.

Zhang, T., Baumjohann, W., Russell, C., Luhmann, J., & Xiao, S. (2016). Weak, quiet magnetic fields seen in the venus atmosphere. *Scientific Reports*, *6*, 23537. https://doi.org/10.1038/srep23537

Zhao, Y.-H., Zimmerman, M. E., & Kohlstedt, D. L. (2009). Effect of iron content on the creep behavior of olivine: 1. Anhydrous conditions. *Earth and Planetary Science Letters*, *287*(1–2), 229–240. https://doi.org/10.1016/j.epsl.2009.08.006